

Probing the Reaction Mechanisms Involved in the Decomposition of Solid 1,3,5-Trinitro-1,3,5-triazinane by Energetic Electrons

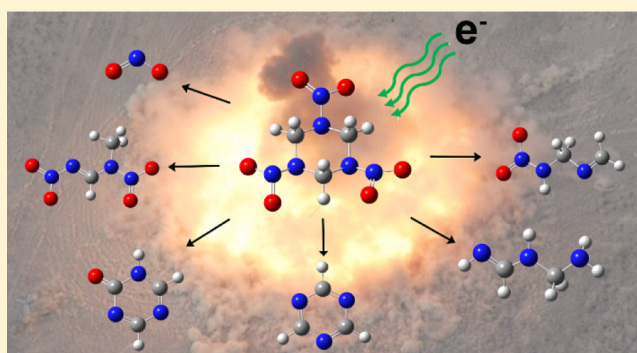
Santosh K. Singh,^{†,‡} Cheng Zhu,^{†,‡} Vasant Vuppuluri,[§] Steven F. Son,[§] and Ralf I. Kaiser^{*,†,‡,§}

[†]Department of Chemistry and [‡]W. M. Keck Research Laboratory in Astrochemistry, University of Hawaii, Honolulu, 96822 Hawaii, United States

[§]Mechanical Engineering, Purdue Energetics Research Center, Purdue University, 500 Allison Road, West Lafayette, Indiana 47907-2088, United States

S Supporting Information

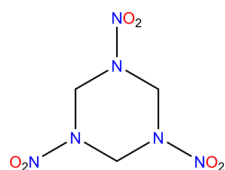
ABSTRACT: The decomposition mechanisms of 1,3,5-trinitro-1,3,5-triazinane (RDX) have been explored over the past decades, but as of now, a complete picture on these pathways has not yet emerged, as evident from the discrepancies in proposed reaction mechanisms and the critical lack of products and intermediates observed experimentally. This study exploited a surface science machine to investigate the decomposition of solid-phase RDX by energetic electrons at a temperature of 5 K. The products formed during irradiation were monitored online and in situ via infrared and UV–vis spectroscopy, and products subliming in the temperature programmed desorption phase were probed with a reflectron time-of-flight mass spectrometer coupled with soft photoionization at 10.49 eV (ReTOF-MS-PI). Infrared spectroscopy revealed the formation of water (H₂O), carbon dioxide (CO₂), dinitrogen oxide (N₂O), nitrogen monoxide (NO), formaldehyde (H₂CO), nitrous acid (HONO), and nitrogen dioxide (NO₂). ReTOF-MS-PI identified 38 cyclic and acyclic products arranged into, for example, dinitro, mononitro, mononitroso, nitro–nitroso, and amines species. Among these molecules, 21 products such as *N*-methylnitrous amide (CH₄N₂O), 1,3,5-triazinane (C₃H₉N₃), and *N*-(aminomethyl)methanediamine (C₂H₉N₃) were detected for the first time in laboratory experiments; mechanisms based on the gas phase and condensed phase calculations were exploited to rationalize the formation of the observed products. The present studies reveal a rich, unprecedented chemistry in the condensed phase decomposition of RDX, which is significantly more complex than the unimolecular gas phase decomposition of RDX, thus leading us closer to an understanding of the decomposition chemistry of nitramine-based explosives.



1. INTRODUCTION

Nitramine-based (N–NO₂) energetic materials such as 1,3,5-trinitro-1,3,5-triazinane (RDX) (Scheme 1) have been widely

Scheme 1. Molecular Structure of RDX



exploited as explosives and propellants.^{1–3} Therefore, over the past decades, extensive studies have been performed to understand the fundamental decomposition mechanisms and the combustion behavior of RDX.^{1–47} These investigations are very much required by the energetic material community to unravel the mechanism along with initial and higher-order bond breaking processes, which trigger the decomposition of energetic molecules such as nitramines. Our current under-

standing of the reaction mechanisms involved in the decomposition of RDX is based on extensive experimental as well as computational studies performed in the gas-phase and in the condensed-phase (Table 1).^{4–37} Gas-phase studies predicted the N–NO₂ bond fission as the initial step in the unimolecular decomposition of RDX.^{6–8,10} For instance, the photodissociation of supersonic jet-cooled RDX at 226 nm revealed the formation of nitrogen monoxide (NO) as the decomposition product via rapid predissociation of nitrogen dioxide (NO₂) with the latter being released by the initial N–NO₂ bond rupture.^{6,10} However, infrared multiphoton dissociation (IRMPD) studies of RDX in a jet-cooled molecular beam proposed a different mechanism.⁹ This study elucidated a concerted, symmetric triple dissociation of the RDX-ring, producing three molecules of methylene nitramine (CH₂NNO₂) as the dominant decomposition pathway in

Received: September 12, 2019

Revised: October 4, 2019

Published: October 7, 2019

Table 1. Molecular Formula, Mass, and Ionization Energies of Decomposition Products of RDX Previously Reported in Gas-Phase and Condensed-Phase Studies

method	products observed				references
	formula	name	mass (amu)	IE (eV)	
photodissociation of RDX at 225 nm in supersonic jet	NO	nitrogen monoxide	30	9.26	Im and Bernstein ⁸
photodissociation at 226 nm in supersonic jet	NO	nitrogen monoxide	30	9.26	Guo et al. ⁷
photodissociation at 226 nm in supersonic jet	NO	nitrogen monoxide	30	9.26	Lemire et al. ¹⁰
	NO ₂	nitrogen dioxide	56	8.80	
IR multiphoton dissociation in molecular beam	HCN	hydrogen cyanide	27	13.59	Zhao et al. ⁹
	CO	carbon monoxide	28	14.01	
	NO	nitrogen monoxide	30	9.26	
	H ₂ CO	formaldehyde	30	10.88	
	CH ₂ NN	diazomethane	42	8.99	
	N ₂ O	nitrous oxide	44	12.77	
	CO ₂	carbon dioxide	44	13.77	
	NO ₂	nitrogen dioxide	46	8.80	
	HONO	nitrous acid	47		
	C ₂ H ₄ N ₂		56		
	CH ₂ N ₂ O ₂		74		
	C ₃ H ₃ N ₃	s-triazene	81	10.00	
	C ₃ H ₄ N ₃		82		
	C ₃ H ₅ N ₃		83		
	C ₂ H ₄ N ₃ O ₂		102		
	CH ₂ N ₃ O ₄		120		
	C ₂ H ₄ N ₄ O ₃		132		
	C ₂ H ₃ N ₄ O ₄		148		
shockwave decomposition	NO ₂	nitrogen dioxide	56	8.80	Miao et al. ²⁵
	HONO	nitrous acid	47		
thermal decomposition	H ₂ O	water	18	12.80	Behrens and Bulusu ⁴
	NO	nitrogen monoxide	30	9.26	
	CH ₂ O	formaldehyde	30	10.88	
	NCO		42		
	N ₂ O	nitrous oxide	44	12.77	
	NO ₂	nitrogen dioxide	46	8.80	
	(CH ₃)NHCHO	N-methylformamide	59	9.50	
	C ₃ H ₃ N ₃ O	oxo-s-triazine	97		
	C ₂ H ₄ N ₄ O ₃		132		
thermal decomposition	H ₂ O	water	18	12.80	Maharrey and Behrens ²⁴
	HCN	hydrogen cyanide	27	13.59	
	CO	carbon monoxide	28	14.01	
	CH ₂ O	formaldehyde	30	10.88	
	NO	nitrogen monoxide	30	9.26	
	N ₂ O	nitrous oxide	44	12.77	
	H ₂ NCHO	N-formamide	45	10.20	
	NO ₂	nitrogen dioxide	46	8.80	
	HONO	nitrous acid	47		
	(CH ₃) ₃ N	trimethyl amine	59	7.80	
	(CH ₃)NHCHO	N-methyl formamide	59	9.05	
	C ₂ H ₂ N ₂ O		70		
	(CH ₃) ₂ NCHO	N,N-dimethyl formamide	73	9.55	
	(CH ₃) ₂ NNO	N-nitroso dimethylamine,	74	8.69	
	C ₃ H ₃ N ₃	s-triazene	81	10.00	
	C ₃ H ₃ N ₃ O	oxo-s-triazine	97		
	C ₃ H ₄ N ₄ O ₂		128		
	C ₃ H ₆ N ₆ O ₅	ONDNTA	206		
CO ₂ laser pyrolysis	HCN	hydrogen cyanide	27	13.59	Botcher and Wight ²⁷
	NO	nitrogen monoxide	30	8.80	
	N ₂ O	nitrous oxide	44	12.77	
	CO ₂	carbon dioxide	44	13.77	
	N ₂ O ₄	nitrogen dioxide dimer	92		
CO ₂ laser pyrolysis and combustion	H ₂	hydrogen molecule	2	15.44	Lee et al. ²⁸
	H ₂ O	water	18	12.80	

Table 1. continued

method	products observed			references	
	formula	name	mass (amu)		IE (eV)
thermal decomposition: flash—heating	HCN	hydrogen cyanide	27	13.59	Gongwer and Brill ²⁹
	CO	carbon monoxide	28	14.01	
	H ₂ CNH	methyleneimine	29	9.90	
	NO	nitrogen monoxide	30	9.26	
	H ₂ CO	formaldehyde	30	10.88	
	HNCO	isocyanic acid	43		
	N ₂ O	nitrous oxide	44	12.77	
	NO ₂	nitrogen dioxide	46	8.80	
	C ₂ H ₄ N ₂	diazaethane	56		
	HONO	nitrous acid	47		
	C ₂ H ₂ N ₂	iminoacetonitrile	54	11.60	
	C ₂ H ₂ N ₂ O		70		
	C ₃ H ₃ N ₃	<i>s</i> -triazene	81	10.00	
	C ₃ H ₃ N ₃ O	oxo-triazine	97		
	HNCO	isocyanic acid	43	11.60	
	HONO	nitrous acid	47		
photodissociation at 248 nm	C ₂ H ₃ NO ₂	C-hydroxy- <i>N</i> -methylformamide	75		Capellos et al. ³⁰
	C ₃ H ₃ N ₃	<i>s</i> -triazene	81	10.0	
	OH	hydroxyl radical	17		
photodissociation at 248 nm	NO	nitrogen monoxide	30	9.26	Dickinson et al. ³⁴
	NO ₂	nitrogen dioxide	46	8.80	
	H ₂	hydrogen	2	15.44	
photolysis at 266 nm	OH	hydroxyl radical	17	13.6	Tang et al. ³¹
	H ₂ O	water	18	12.80	
	HCN	hydrogen cyanide	27	13.59	
	H ₂ CO	formaldehyde	30	10.88	
	NO	nitrogen monoxide	30	9.26	
	CH ₂ NN	diazomethane	42	9.00	
	C ₂ H ₄ N	ethanenitrilium	42		
	N ₂ O	nitrous oxide	44	12.77	
	C ₂ H ₄ N	ethanenitrilium	45		
	NO ₂	nitrogen dioxide	46	8.80	
	CH ₂ CH ₂ N ₂	diazoethane	56		
	CH ₂ NNO ₂	methylene nitramine	74		
	C ₃ H ₃ N ₃	<i>s</i> -triazene	81	10.0	
	O	nascent oxygen	16		
	OH	hydroxyl radical	17	13.6	
	CN	cyanide radical	26		
photolysis at 229 nm	HCN	hydrogen cyanide	27	13.59	Gares et al. ³³
	NCN	cyanonitrene	40		
	CHNN	diazomethane radical	41		
thermal decomposition at high temperature and pressure	CH ₂ NN	diazomethane	42	9.00	Connor et al. ³⁸
	NO ₂	nitrogen dioxide	46	8.80	
	NO ₂	nitrogen dioxide	46	8.80	
radiation-induced decomposition in solution	CO ₂	carbon dioxide	44		Markarov et al. ²⁶
	N ₂ O	nitrous oxide	44	12.77	
	NO ₂	nitrogen dioxide	46	8.80	
catalytic thermal decomposition	H ₂ O ₂	hydrogen peroxide	34	12.10	Song et al. ³⁹
	CO	carbon monoxide	28	14.01	
	N ₂	nitrogen	28		
photodissociation at 236 nm	N ₂ O	nitrous oxide	44	12.77	Wynn et al. ⁴⁰
	NO ₂	nitrogen dioxide	46	8.80	
	NO fragments	nitrogen monoxide	30	9.26	

contrast to the N–NO₂ bond fission.⁹ On the other hand, IRMPD experiments of RDX performed by Zuckermann et al. in the gas-phase revealed a third decomposition route involving a five-membered ring intermediate, which eventually formed

hydroxyl (OH) radicals either directly or via dissociation of nitrous acid (HONO).¹¹

Several theoretical calculations have been performed to resolve the aforementioned discrepancies for the gas-phase

decomposition of RDX.^{12–16,18–21} The majority of these calculations favored the homolytic N–NO₂ bond fission over the concerted triple C–N scission mechanism.^{13–18} The energy required for the N–NO₂ homolysis is lower by about 84 kJ mol^{−1} relative to the concerted mechanism.¹⁴ In addition to the most favorable N–NO₂ bond fission, Goddard et al. proposed a new decomposition pathway, which involved three successive molecular eliminations of HONO forming eventually the 1,3,5-triazine (C₃H₃N₃) molecule.¹⁴ Quantum calculations performed by Swadley and Li further confirmed the N–NO₂ bond rupture and HONO elimination reactions as the initial steps in the decomposition of RDX.¹⁵ Harris and Lammertsma proposed that the N–NO₂ homolysis could be followed by hydrogen migration during the decomposition of RDX.¹⁸ In contrast to these three pathways (N–NO₂ bond fission, HONO elimination, concerted triple C–N scission), Im and Bernstein extracted a fourth pathway, where isomerization of one of the nitro (–NO₂) to a nitroso (–ONO) group was considered as an initial route for the unimolecular decomposition of RDX.⁸ Bartlett et al. revealed that the HONO elimination reaction represents the most preferred route at 298 K and 1 atm pressure compared to N–NO₂ homolysis, concerted C–N scission, and nitroso (–ONO) isomerization.¹³ However, *ab initio* molecular dynamics calculation by Schweigert proposed the dominance of N–NO₂ bond rupture over HONO elimination and triple C–N scission mechanism over a temperature range from 1000 to 2000 K.¹⁶

Besides the gas phase, the decomposition of RDX in the solid as well as liquid phase was explored by exploiting thermal energy, shock waves, and laser irradiation.^{4,24–34} For example, thermal decomposition of RDX was investigated by Behrens and Bulusu using simultaneous thermogravimetric modulated beam mass spectrometry at a temperature above and below the melting point of RDX (478 K).^{4,5} These authors observed several products such as water (H₂O), hydrogen cyanide (HCN), carbon monoxide (CO), formaldehyde (H₂CO), nitrogen monoxide (NO), dinitrogen oxide (N₂O), formamide (NH₂CHO), nitrogen dioxide (NO₂), nitrous acid (HONO), *N*-methylformamide ((CH₃)NHCHO), oxy-*s*-triazine (C₃H₃N₃O; OST), and 1-nitroso-3,5-dinitrohexahydro-*s*-triazine (ONDNTA; C₃H₆N₆O₅).^{4,24} The authors proposed that ONDNTA is formed during the early stage of the decomposition; this molecule subsequently decomposed to dinitrogen monoxide (N₂O) and formaldehyde (H₂CO).⁴ However, the authors did not observe any primary intermediates in the experiments. Thermal decomposition studies of RDX further showed that during decomposition, increase in NO₂ and oxygen content inhibits the decomposition processes by removing the products such as hydroxymethyl formamide ((OH)CH₂NHCHO) and formaldehyde (H₂CHO), which act as catalysts for thermal decomposition.^{44–47} Furthermore, shock wave decomposition of RDX crystals at pressures lower than 10 GPa revealed that the decomposition pathways leading to the formation of NO₂ and HONO were dominant. However, stresses higher than 10 GPa resulted in dominance of reaction between pristine radicals generated and unreacted RDX.²⁵ Wight and Botcher studied the laser pyrolysis of RDX at 77 K.²⁷ Their observation of dinitrogen tetroxide (N₂O₄) during the initial stage of the decomposition proposed that the N–NO₂ bond fission was likely the primary pathway. Laser pyrolysis of RDX was also studied at 293 K; the authors observed hitherto higher

molecular weight species with mass-to-charge (*m/z*) values of 47 (HONO), 54 (C₂H₂N₂), 56 (C₂H₂N₂), 70 (C₂H₂N₂O), 81 (C₃H₃N₃), and 97 (C₃H₃N₃O).²⁸ UV-photolysis of RDX crystals were explored at distinct wavelengths.^{30,31,33,34} Photolysis at 248, 236, and 229 nm predominantly produced NO₂, which further supports the N–NO₂ bond fission to be the primary route for the decomposition of RDX.^{30,34} Exposure to 266 nm resulted in successive NO₂ losses, ring opening to form nitrogen-bearing species along with highly unsaturated molecules carrying C=N moieties.³¹ Molecular dynamics simulations revealed the formation of NO₂ via N–NO₂ bond rupture, HONO elimination, and fragmentation to methylene nitramine (CH₂NNO₂).^{35–37}

In summary, condensed phase studies exposed a significantly richer and more complex chemistry as evidenced in higher molecular weight products, which were not observed in the gas phase conditions. It is important to mention that the majority of the thermal decomposition studies of RDX were carried out in a temperature range from 443 to 573 K.^{4,24} At these temperatures, the reactive intermediates formed during the decomposition may undergo rapid decomposition to secondary products; likewise, the initially formed carbon-, oxygen-, and nitrogen-centered radicals can react further.²⁷ Therefore, a complete picture and a consistent decomposition mechanism of condensed phase RDX has not yet emerged. Here, we employed a surface science machine to explore the decomposition of RDX in the condensed phase (solid) via energetic electrons. The sample is kept at 5 K during the exposure, thus eliminating the escape of any volatile products into the gas phase. The products are identified via Fourier transform infrared (FTIR) and ultraviolet–visible (UV–vis) spectroscopy (condensed phase) and by a reflectron time-of-flight mass spectrometer coupled with vacuum ultraviolet (VUV) photoionization (PI-ReTOF-MS) during the temperature programmed desorption (TPD). This technique has been used previously to study the decomposition mechanism of nitromethane (CH₃NO₂), which is considered as the simplest model compound of nitrohydrocarbon-based energetic materials.^{48–51} Our study on the decomposition of RDX revealed 21 previously unobserved intermediates. Most significantly, the observation of mononitroso intermediates proposes the existence of ONDNTA decomposition product. Our results also show evidence of reactive radical species previously only predicted computationally, but not observed in experiments as reactive intermediates. On the basis of our observations, we propose comprehensive decomposition pathways of RDX in the condensed phase.

2. EXPERIMENTAL SECTION

2.1. Experimental. The experiments were carried out in an ultrahigh vacuum (UHV) chamber evacuated to a pressure of typically 2×10^{-10} Torr, exploiting oil-free turbomolecular pumps backed by dry scroll pumps.^{52–54} A polished silver wafer (substrate) coated with a film of RDX of thickness of 16.8 ± 1.0 μm is sandwiched with indium foil and interfaced to a cold finger manufactured from oxygen-free high conductivity copper. This assembly is connected to a UHV compatible closed cycle helium refrigerator (Sumitomo Heavy Industries, RDK-415E) which cools down the temperature of the substrate to 5.0 ± 0.1 K. The temperature of the substrate can be controlled with the help of a cartridge heater. This system is freely rotatable horizontally and translatable vertically exploiting a differently pumped rotary feedthrough (Ther-

moionics Vacuum Products, RNN-600/FA/MCO). Infrared (IR) spectra of the RDX film were collected in situ at 5 K in the 4000–600 cm^{-1} region using a FTIR spectrometer (Nicolet 6700) operated at a resolution of 4 cm^{-1} . All FTIR measurements were performed in an absorption–reflection–absorption geometry at an angle of 45° to the normal of the substrate (Figures 1, 2, and Table 3). The thickness of the

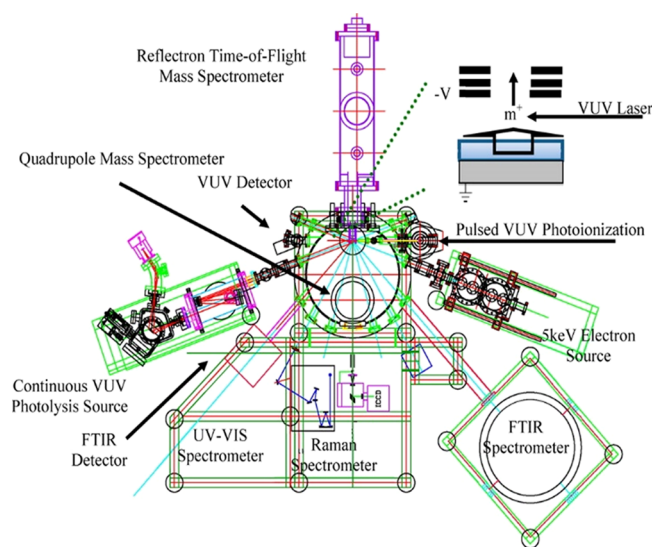


Figure 1. Schematic top view of the ultrahigh vacuum chamber including the radiation sources (electron source), analytical instruments (FTIR, UV–vis, ReTOF), and cryogenic target (point of convergence lines). Adapted with permission from ref 51. Copyright (2015) Royal Society of Chemistry.^{52–54}

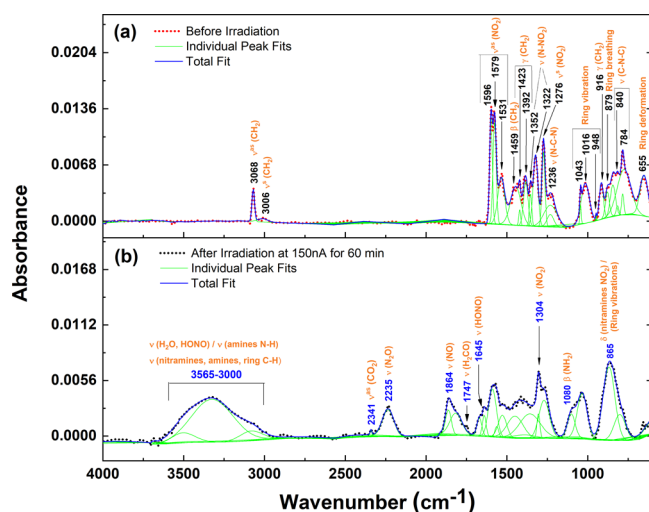


Figure 2. IR spectra of RDX collected at 5 K (a) before and (b) after irradiation of the high dose experiment.

RDX film was determined based on interference patterns observed in the IR spectrum due to fringing effect via eq 1

$$d = \frac{N}{2\sqrt{n^2 - \sin^2 \theta}(\nu_1 - \nu_2)} \quad (1)$$

where d is the thickness of the film, N is the number of fringes in the spectral region from ν_1 to ν_2 cm^{-1} , n is the refractive index of RDX ($n = 1.49$),⁵⁵ θ is the angle of incidence, and ν_1 and ν_2 are the start and end points of the spectrum in cm^{-1}

covering the fringes. The UV–vis spectra of the RDX films were also recorded in situ at 5 K covering the range from 190 to 800 nm using a modified UV–vis spectrophotometer (Evolution 600). All UV–vis measurements were performed at an angle of 30° relative to the normal of the substrate. After the reference spectra of the unirradiated RDX samples were taken, each RDX film was exposed to energetic electrons (5 keV) at an angle of 0° relative to the normal of sample surface, at two different electron currents of 20 ± 2 nA for 30 min (low dose) and 150 ± 2 nA for 60 min (high dose) by scanning the electron beam over an area of 1.0 ± 0.1 cm^2 . IR spectra of the RDX films were collected in situ before and after irradiation to monitor the changes induced by the ionizing radiation inside the films. Monte Carlo simulations via the CASINO 2.42 software⁵⁶ were performed to determine electron penetration depth and the average energy deposited on the RDX-film (Table 2). The average penetration depth of the electrons is

Table 2. Data Applied to Calculate the Average Dose per RDX Molecule for the Low and High Dose Experiments

	(a)	(b)
initial kinetic energy of the electrons	5 keV	5 keV
irradiation current (I)	20 ± 2 nA	150 ± 2 nA
irradiation time (t)	1800 s	3600 s
average penetration depth, l	267 ± 80 nm	267 ± 80 nm
average kinetic energy of backscattered electrons, E_{bs}^a	3.6 ± 0.3 keV	3.6 ± 0.3 keV
fraction of backscattered electrons, f_{bs}^a	0.6 ± 0.1	0.6 ± 0.1
average kinetic energy of transmitted electrons, E_{trans}^a	0.0 keV	0.0 keV
fraction of transmitted electrons, f_{trans}^a	0	0
density of the ice, ρ	1.82 g cm^{-3}	1.82 g cm^{-3}
irradiated area, A	1.0 ± 0.1 cm^2	1.0 ± 0.1 cm^2
total number of molecules processed	$(1.1 \pm 0.2) \times 10^{18}$	$(1.6 \pm 0.2) \times 10^{19}$
dose per molecule, D	8.1 ± 1.0 eV	100 ± 16 eV
total number of electrons	$(2.3 \pm 1.0) \times 10^{14}$	$(3.4 \pm 1.0) \times 10^{15}$

^aValues from CASINO simulations.

calculated to be 267 ± 80 nm with averages doses of 8.1 ± 1.0 and 100 ± 16 eV per molecule for the low dose and high dose experiments, respectively. The penetration depth of the electron is less than the thickness of the RDX film guaranteeing that the electron beam does not interact with the silver substrate.

After irradiation, the exposed samples were annealed from 5 to 320 K at a rate of 1 K min^{-1} (TPD). During the TPD, the products subliming from the substrate were analyzed, exploiting photoionization reflectron time-of-flight mass spectrometry (PI-ReTOF-MS). Details of the PI-ReTOF-MS setup have been described previously.^{53,54,57–59} In brief, we exploited pulsed VUV light at 10.49 eV to softly photoionize the subliming molecules. These ions are extracted and eventually detected in the reflectron time-of-flight tube based on their mass-to-charge (m/z) ratios prior to reaching the microchannel plate (MCP) detector (Jordan TOF Products Inc.). The signal generated by MCP detector is amplified using a pre-amplifier (Ortec 9305) and shaped with a 100 MHz discriminator (Advanced Research Instruments Corporation; F-100TD). A computer-based multichannel scaler (FAST ComTec, P7888-1 E) receives the signal from the discrim-

inator and records it in 4 ns bins triggered at 30 Hz by a pulse delay generator (Quantum Composers 9518). 3600 sweeps are collected per mass spectrum per 1 K increase during the TPD phase.

2.2. Sample Preparation. RDX samples were received from BAE Systems, Inc. prepared according to the MIL-DTL-398 D (Military Specification, Detail Specification RDX, 12 DEC 1996); this specifies an HMX (1,3,5,7-tetranitro-1,3,5,7-tetrazoctane; $C_4H_8N_8O_8$) impurity in RDX at levels from 4 to 17%. The maximum permissible quantity of other impurities if present is 0.08%. In order to remove the impurities, production grade RDX was recrystallized from acetone (Fisher Scientific, Inc.). Nuclear magnetic resonance (NMR) spectroscopy was exploited to characterize the recrystallized RDX. Figure S1 of the Supporting Information shows the ^{13}C NMR spectra of the crude and recrystallized RDX measured using a Spinsolve 60 Carbon benchtop 60 MHz NMR spectrometer after dissolving in dimethylsulfoxide- d_6 solvent. The disappearance of the peaks associated with the chemical shift of HMX indicates that RDX has been sufficiently purified to a level of at least 99.9%.⁶⁰ A thin film of RDX onto the silver substrate was prepared using a drop-casting method. For the drop-casting, about 2 mg of recrystallized (purified) RDX is dissolved in 3 g of methyl ethyl ketone (MEK; Acros Organics) inside a vial. Sonication and mild heating at 305 K ensure complete dissolution of the RDX in MEK. Using a glass pipette, a drop of RDX/MEK solution was deposited onto the silver substrate and then left for drying. A uniform layer of RDX is observed after the evaporation of solvent and characterized via IR spectroscopy (Section 3.1).

3. RESULTS AND DISCUSSION

3.1. IR Spectroscopy. **3.1.1. Qualitative Analysis.** Figure 2a,b displays the IR spectra of RDX before and after irradiation in the region from 4000 to 600 cm^{-1} . Detailed assignments of the observed IR bands are provided in Table 3. The IR spectrum of RDX reveals prominent NO_2 stretch, N–N stretch, CH_2 -bending, and ring vibrational bands in the region 1600–600 cm^{-1} along with CH_2 -stretches in the 3100–3000 cm^{-1} region; these findings are in excellent agreement with the IR spectrum of RDX reported in the literature.^{61,62} The thin film of RDX can exist in a crystalline or amorphous phase. The crystalline form of RDX shows sharp IR bands with narrow band width, whereas the amorphous phase of RDX exhibits broad and diffuse bands.²⁷ The IR spectra of the RDX film measured in the present study and that of the crystalline phase recorded by Botcher et al. are compared in Figure S2 of the Supporting Information. Figure S2 unveils that the thin film of RDX used in this work is amorphous. The fundamentals at 3068 and 3006 cm^{-1} correspond to the CH_2 asymmetric and symmetric stretching modes, respectively. The CH_2 bending modes (in-plane and out-of-plane) are observed in the spectral range from 1450 to 1380 cm^{-1} . A group of three bands at 1596, 1579, and 1531 cm^{-1} can be attributed to the antisymmetric stretching modes of the $-NO_2$ group. The characteristic N– NO_2 stretching vibrations of RDX appear at 1352 and 1322 cm^{-1} . The spectral regions 1240–1210, 1050–950, and 880–600 cm^{-1} are dominated by ring vibrations. Bands observed in the region 1240–1210 cm^{-1} are linked to the N–C–N stretching modes of the ring. The symmetric vibration mode of the ring—also known as ring breathing—appear at 879 cm^{-1} ; bands at 840 and 784 cm^{-1} are attributed to C–N–C stretching vibrations.

Table 3. (a) IR Features of RDX before the Irradiation along with (b) New Bands Observed in the Spectrum in the High Dose Experiment at 5 K

wavenumber observed (cm^{-1})	wavenumber literature (cm^{-1}) ⁶²	vibrational assignments	vibrational modes
(a) Before Irradiation			
3068	3068	$\nu^{as}(CH_2)$	C–H asymm stretch
3006	3004	$\nu^s(CH_2)$	C–H symm stretch
1596	1593	$\nu^{as}(NO_2)$	NO_2 asymm stretch
1579	1576	$\nu^{as}(NO_2)$	NO_2 asymm stretch
1531	1535	$\nu^{as}(NO_2)$	NO_2 asymm stretch
1459	1460	$\beta(CH_2)$	CH_2 bending in plane
1435	1435	$\beta(CH_2)$	CH_2 bending in plane
1423	1424	$\gamma(CH_2)$	CH_2 bending out of plane
1392	1391	$\gamma(CH_2)$	CH_2 bending out of plane
1352	1352	$\nu^s(N-NO_2)$	N–N symm stretch
1322	1322	$\nu^s(N-NO_2)$	N–N symm stretch
1276	1275	$\nu^s(NO_2)$	NO_2 symm stretch
1236	1232	$\nu(N-C-N)$	ring skeletal vibrations
1218	1219	$\nu(N-C-N)$	ring skeletal vibrations
1043	1040	$\nu^{as}(\text{ring})$	ring asymm vibrations
1016	1020	$\nu^{as}(\text{ring})$	ring asymm vibrations
948	947	$\nu^{as}(\text{ring})$	ring asymm vibrations
916	917	$\gamma(CH_2)$	CH_2 bending out of plane
879	882	$\nu^s(\text{ring})$	ring symm vibration
840	844	$\nu(C-N-C)$	ring skeletal vibrations
784	790	$\nu(C-N-C)$	ring skeletal vibrations
655	670	$\delta(\text{ring})$	ring deformation
(b) After Irradiation			
3565–3000		$\nu(H_2O)$	O–H stretch of H_2O
		$\nu(HONO)$	O–H stretch of HONO
		$\nu(NH_2)$	N–H stretch of amines
		$\nu(CH_2NNO_2)$	C–H stretch of nitramines
2341		$\nu(NH_2)$	C–H stretch of amines
		ring	C–H stretch of ring
	2342 ²⁷	$\nu(CO_2)$	C=O stretch of CO_2
	2235	$\nu(N_2O)$	N=N stretch of N_2O
1864	1864 ²⁷	$\nu(NO)$	free NO stretch
1747	1742 ⁶³	$\nu(H_2CO)$	C=O stretch of formaldehyde
1645	1640 ⁶⁴	$\nu(HONO)$	N=O stretch of HONO
1304	1304 ⁷¹	$\nu(NO_2)$	N=O stretch of NO_2
1080		$\beta(NH_2)$	NH_2 bending modes of amine
865	871 ²⁷	$\delta(NNO_2)/\nu(\text{ring})$	deformation modes of nitramines/ring vibrations

The IR spectrum after irradiation is distinct from the data obtained for the pure RDX sample (Figure 2b); the fundamentals of RDX decrease in column density by $40 \pm 10\%$ (low dose) and $72 \pm 14\%$ (high dose); new bands appear in the region 3565–3000, 2341, 2235, 1864, 1747, 1645, 1304, 1080, and 865 cm^{-1} . These new features can be assigned to primary and secondary decomposition products of RDX. Bands at 2341, 2235, 1864, and 1747 cm^{-1} can be associated with stretching vibrations of carbon dioxide (CO_2), dinitrogen oxide (N_2O), nitrogen monoxide (NO), and formaldehyde (H_2CO), respectively. Absorptions corresponding to second-

dary products (CO_2 , N_2O , NO , and H_2CO) have been observed by Botcher and Wight and Alix and Collins during decomposition of RDX via laser pyrolysis and photolysis.^{27,63} The band observed at 1645 cm^{-1} can be allocated to the fundamental $\text{N}=\text{O}$ stretch of HONO, which is in good agreement with the 1640 cm^{-1} assigned previously to the cis conformer of HONO.⁶⁴

Further, the characteristic symmetric stretching vibration of NO_2 is observed at 1304 cm^{-1} , which matches nicely with the reported literature value of 1304 cm^{-1} .⁷¹ The asymmetric stretching vibration of NO_2 (1613 cm^{-1}) is masked by the broad absorption feature of $\text{RDX}-\text{NO}_2$ (stretching vibrations; $1600\text{--}1520\text{ cm}^{-1}$). We also observe a feature at 1080 cm^{-1} , merged with the absorption band of RDX; this can be tentatively assigned to the bending mode of amines ($-\text{NH}_2$).^{65–67} The absorption band observed at 865 cm^{-1} could be linked to the decomposition, product methylene nitramine (CH_2NNO_2) based on its calculated vibrational frequencies reported by Mowrey et al.⁶⁸ This assignment is tentative as it is merged with the ring vibrations of RDX. In fact, probing the formation of methylene nitramine (CH_2NNO_2) during RDX decomposition is difficult via IR spectroscopy as most of its vibrational bands are obscured by the absorption bands of RDX.²⁷ It is also important to highlight that evidence of formation of HONO, NO_2 , and amines ($-\text{NH}_2$) from the decomposition of RDX have not been reported previously through IR spectroscopy. Their signatures have been reported only through mass spectrometry.^{4,9,24} Figure 2b also shows broad absorption band covering the spectral range from 3565 to 3000 cm^{-1} . This broad feature is due to multiple vibrations in the region $3565\text{--}3000\text{ cm}^{-1}$, which include the O–H stretch (H_2O , HONO), N–H stretch (amines), and C–H stretch (amines, nitramines, ring).^{64,65,67–69}

3.1.2. Quantitative Analysis: Mass Balance. The column densities were calculated using a modified Lambert–Beer law to determine the amount of RDX molecules destroyed and that of products formed.⁷⁰ The integrated absorption coefficient of the reactant and products used for the calculation of column densities are taken from the literature. The absorption coefficient of the RDX band at 1596 cm^{-1} is $1.0 \times 10^{-18}\text{ cm molecule}^{-1}$. The integrated band strength of the stretching mode of NO_2 (1304 cm^{-1}) is $6.2 \times 10^{-18}\text{ cm molecule}^{-1}$.⁷¹ The $\text{N}=\text{O}$ stretch of NO (1864 cm^{-1}) and HONO (1645 cm^{-1}) hold integrated band strengths of 6.8×10^{-18} and $7.2 \times 10^{-18}\text{ cm molecule}^{-1}$ respectively, whereas the $\text{N}=\text{N}$ stretch of N_2O (2235 cm^{-1}) has an absorption coefficient of $5.7 \times 10^{-17}\text{ cm molecule}^{-1}$.^{70–72} Carbon dioxide (CO_2) was quantified via the stretching mode (2341 cm^{-1}), which has an absorption coefficient of $7.6 \times 10^{-17}\text{ cm molecule}^{-1}$.⁵¹ The column density of H_2O (water) is measured in the region of $3500\text{--}3100\text{ cm}^{-1}$ using an integrated band strength of $2.0 \times 10^{-16}\text{ cm molecule}^{-1}$.⁷³ It is important to note here that the broad absorption in the region $3567\text{--}3000\text{ cm}^{-1}$ includes O–H stretch of HONO, amines N–H stretch, and ring C–H stretch along with O–H stretch of H_2O . Therefore, to determine the column density of water, only region $3500\text{--}3100\text{ cm}^{-1}$ is considered where the O–H stretch of H_2O has maximum absorption. The amount of RDX molecules destroyed via radiolysis (high dose) is $1.3 \pm 0.3 \times 10^{16}\text{ molecules cm}^{-2}$, that is 72% of the initial column density ($1.8 \pm 0.3 \times 10^{16}\text{ molecules cm}^{-2}$). On the other hand, the total number of molecules of NO_2 ($4.5 \pm 0.4 \times 10^{14}\text{ molecules cm}^{-2}$), HONO

($4.4 \pm 0.4 \times 10^{14}\text{ molecules cm}^{-2}$), NO ($1.5 \pm 0.2 \times 10^{14}\text{ molecules cm}^{-2}$), CO_2 ($2.6 \pm 0.3 \times 10^{13}\text{ molecules cm}^{-2}$), N_2O ($7.1 \pm 0.7 \times 10^{13}\text{ molecules cm}^{-2}$), and H_2O ($6.0 \pm 0.6 \times 10^{14}\text{ molecules cm}^{-2}$) accounts for only $9 \pm 1\%$ of the decomposed RDX molecules. Therefore, we can conclude that nearly 90% of RDX molecules decomposes into products, which remained unobserved via IR spectroscopy due to overlapping fundamentals with the RDX reactant.

In summary, our IR spectroscopic studies provide clear evidence of formation of critical decomposition products such as water (H_2O), carbon dioxide (CO_2), dinitrogen oxide (N_2O), nitrogen monoxide (NO), formaldehyde (H_2CO), nitrous acid (HONO), and nitrogen dioxide (NO_2) after irradiation of RDX (Figure 3). Although, the presence of

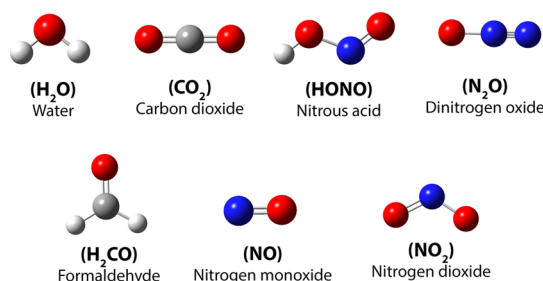


Figure 3. Structures of the decomposition products detected through FTIR spectroscopy.

primary products such as methylene nitramine (CH_2NNO_2), amines, and cyclic as well as acyclic intermediates cannot be unraveled with absolute certainty through FTIR spectroscopy due to functional groups overlapping with RDX, their existence is inferred indirectly based on the appearance of broad absorption bands in the region $3565\text{--}3000$, $1100\text{--}1000$, and $950\text{--}850\text{ cm}^{-1}$, where vibrational frequencies of amines, nitramines, and ring vibrations are observable.

3.2. UV–Vis Spectroscopy. Figure 4 shows the UV–vis spectra of the RDX film measured before and after irradiation

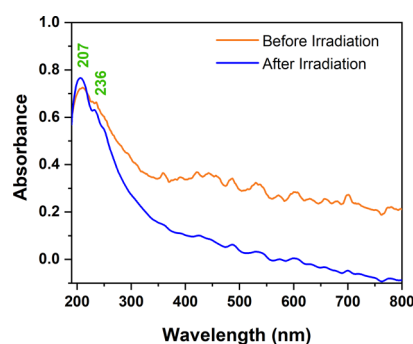


Figure 4. UV–vis spectra of RDX collected at 5 K before and after the high dose.

in the spectral range of $190\text{--}800\text{ nm}$. UV–vis spectrum of RDX prior to irradiation displays an absorption maximum at around 207 nm and a shoulder at around 236 nm . The absorption at 207 and 237 nm is primarily due to the $\pi \rightarrow \pi^*$ transition from the nitro group; the broad absorption around 236 nm has contributions from the weak $n \rightarrow \pi^*$ transition.^{74,75} After irradiation, a decrease in the intensity of the absorption at 236 nm and an increase in the intensity of absorption maxima at 207 nm are observed. Furthermore, the

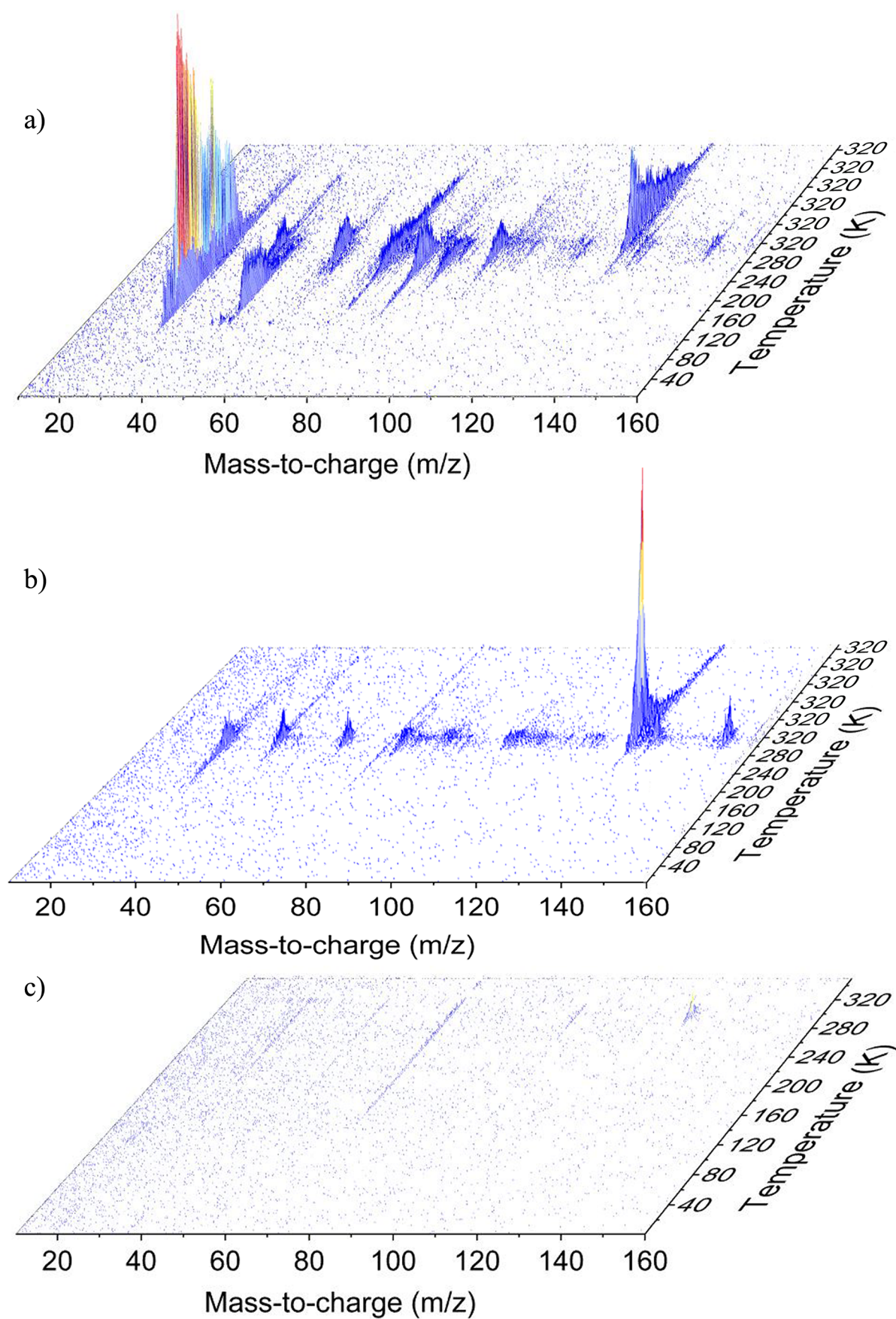
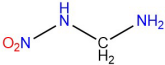
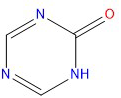
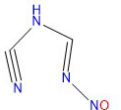
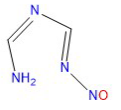
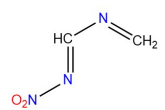
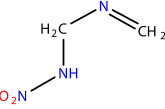
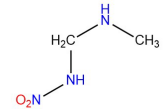
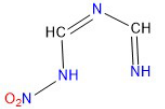
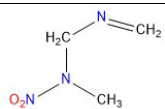
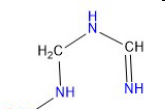
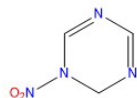
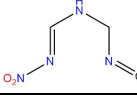
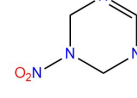
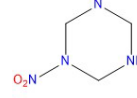
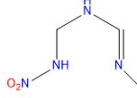
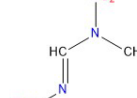
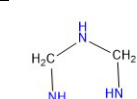


Figure 5. Temperature-dependent ReTOF data of the decomposition products of RDX for the high dose (a), low dose (b), and blank (c) experiments.

Table 4. Molecular Formula, Structure, and Ionization Energies of the Masses Observed in ReTOF Mass Spectrometer via Photoionization at 10.49 eV^a

m/z	Molecular formula	Structure	IE (eV)	Low Dose	High Dose
30	NO		9.26	+	+
31	HNO		10.1		+
	CH ₃ NH ₂		8.90		+
42	CH ₂ N ₂		8.99		+
43	C ₂ H ₅ N		9.30		+
			9.20		+
45	CH ₃ NO		10.16		+
			9.30		+
			10.11		+
46	NO ₂		9.58	+	+
56	C ₂ H ₄ N ₂		8.95	+	+
58	CH ₂ N ₂ O			+	+
	C ₂ H ₆ N ₂			+	+
60	CH ₄ N ₂ O				+
70	C ₃ H ₆ N ₂				+
71	C ₂ H ₅ N ₃			+	+
72	C ₃ H ₈ N ₂			+	+
73	C ₂ H ₇ N ₃			+	+
74	CH ₂ N ₂ O ₂			+	+
75	C ₂ H ₉ N ₃			+	+
81	C ₃ H ₃ N ₃		9.80	+	+
82	C ₃ H ₄ N ₃			+	+
83	C ₃ H ₅ N ₃			+	+
85	C ₃ H ₇ N ₃			+	+
87	C ₃ H ₉ N ₃			+	+
89	CH ₃ N ₃ O ₂			+	+

Table 4. continued

m/z	Molecular formula	Structure	IE (eV)	Low Dose	High Dose
91	CH ₅ N ₃ O ₂			+	+
97	C ₃ H ₃ N ₃ O			+	+
98	C ₂ H ₂ N ₄ O			+	+
100	C ₂ H ₄ N ₄ O			+	+
101	C ₂ H ₃ N ₃ O ₂			+	+
103	C ₂ H ₃ N ₃ O ₂			+	+
105	C ₂ H ₇ N ₃ O ₂			+	+
116	C ₂ H ₄ N ₄ O ₂			+	+
117	C ₃ H ₇ N ₃ O ₂				+
118	C ₂ H ₆ N ₄ O ₂			+	+
128	C ₃ H ₄ N ₄ O ₂			+	+
130	C ₃ H ₆ N ₄ O ₂			+	+
132	C ₃ H ₈ N ₄ O ₂			+	+
148	C ₂ H ₄ N ₄ O ₄			+	+
149	C ₂ H ₇ N ₅ O ₃			+	+
150	C ₂ H ₆ N ₄ O ₄			+	+
157	C ₃ H ₃ N ₅ O ₃			+	+

^aMasses marked with green color were reported previously by both experiment and theoretical calculations, whereas masses marked with blue color are observed only in the previous experimental studies and masses marked with red color are supported only through theoretical calculations reported in the literature.

maximum at around 207 nm is slightly blue-shifted after irradiation. Our UV spectra, measured before and after irradiation of RDX, is in good agreement with that reported by Gares et al. and Makarov et al.^{26,33} The increase in the intensity of the absorption at 207 nm after irradiation is due to accumulation of decomposition products of RDX such as dinitrogen oxide (N₂O), methylene nitramine (CH₂NNO₂), diazomethane (CH₂N₂), and nitrogen dioxide (NO₂) which contribute through their $\pi \rightarrow \pi^*$ transitions to the 207 nm band.³³

3.3. Single Photon Ionization Reflectron Time-of-Flight Mass Spectrometry. To identify individual molecules formed in the decomposition of RDX, single photon ionization reflectron time-of-flight mass spectrometry (PI-ReTOF-MS) was exploited;^{76–83} this approach allows the detection of a broad range of products based on their mass-to-charge ratio (m/z) and sublimation temperature. Figure 5a,b depicts the temperature-dependent mass spectra of the ionized decomposition products of the irradiated RDX samples at the high dose and low dose experiments, respectively. It is apparent that the ion counts of the decomposition products formed after

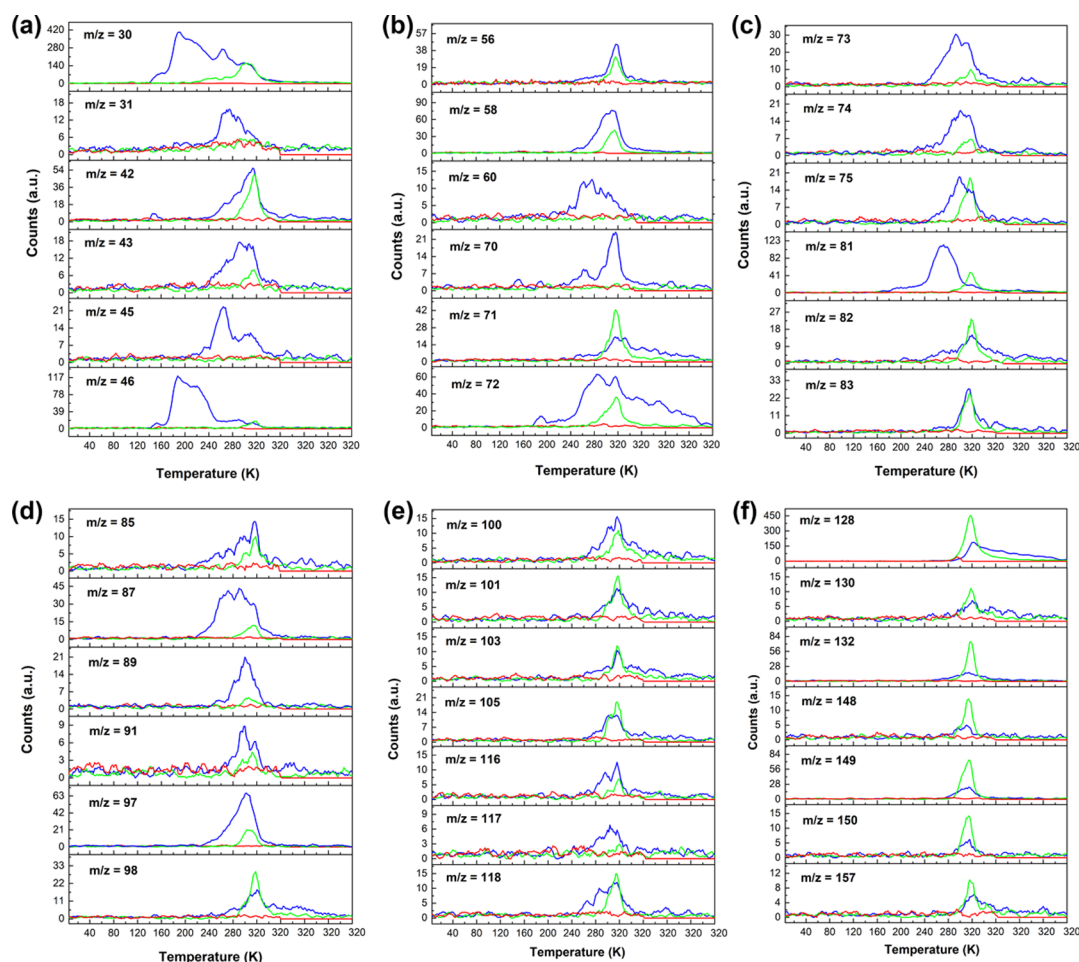


Figure 6. TPD profiles of the ion counts recorded at mass-to-charge ratios of (a) 30, 31, 42, 43, 45, 46, (b) 56, 58, 60, 70, 71, 72, (c) 73, 74, 75, 81, 82, 83, (d) 85, 87, 89, 91, 97, 98, (e) 100, 101, 103, 105, 116, 117, 118, (f) 128, 130, 132, 148, 149, 150, and 157 at a photoionization energy of 10.49 eV. Blue: high dose; green: low dose; red: blank.

irradiation are enhanced with the dose, that is higher ion counts as the dose increases. Furthermore, the ion counts of the lower molecular weight products are enhanced compared to the higher molecular weight species in the high dose experiments, proposing that the initially formed high molecular (possibly primary decomposition) products subsequently decompose to lower molecular products as the dose increases. Overall, we observed species holding mass-to-charge (m/z) values of 30, 31, 42, 43, 45, 46, 56, 58, 60, 70, 71, 72, 73, 74, 75, 81, 82, 83, 85, 87, 89, 91, 97, 98, 100, 101, 103, 105, 116, 117, 118, 128, 130, 132, 148, 149, 150, and 157 in the ReTOF after the high-dose irradiation. All masses are also observed at the low-dose experiment with the exception of $m/z = 31$, 42, 45, 60, 70, and 117. The assigned molecular formulae and potential structures of all these species are shown in Table 4.

It is essential to mention that the ReTOF data collected in blank experiments—experiments conducted in the similar fashion, but without exposing the samples to energetic electrons (Figure 5c)—did not show any signal, which ensures that the decomposition products observed in irradiation experiments are solely due to the impinging ionizing radiation. The corresponding TPD traces are compiled in Figure 6.

Figure 6a shows the TPD profiles of $m/z = 30$, 31, 42, 43, 45, and 46. The ion signal intensities at $m/z = 30$, 43, and 46 are lower by a factor of about three in the low-dose experiments. Signal at $m/z = 30$ can be assigned to nitrogen

monoxide (NO; IE = 9.26 eV), which has been previously observed in the decomposition of RDX.^{4,7,9} Ion signal at $m/z = 31$ can be either assigned to nitrosyl hydride (HNO; IE = 10.1 eV) and/or methylamine (CH_3NH_2 ; IE = 8.90 eV). The maximum of the ion count profile at $m/z = 31$ at 280 K correlates with the second sublimation event recorded at $m/z = 30$ at 280 K. Therefore, ion counts at $m/z = 30$ at around 280 K likely represent fragments of $m/z = 31$ (CH_5N^+ ; HNO^+), that is CH_4N^+ and/or NO^+ . Lossing et al. demonstrated an appearance energy (AE) of AE = 10.18 eV for CH_4N^+ from CH_5N^+ .⁸⁴ Therefore, we may conclude that at least some of the ion counts at $m/z = 31$ and 30 originate from singly ionized methylamine (CH_5N^+) and its CH_4N^+ fragment, respectively. It is important to note that $m/z = 31$ has not been identified in any previous experimental study investigating the decomposition of RDX. Ion signal at $m/z = 42$ can be associated with the molecular formula CH_2NN (diazomethane; IE = 8.99 eV), which has been observed in the previous experimental studies.^{4,9,28,31} Two molecules with the molecular formula $\text{C}_2\text{H}_5\text{N}$ can contribute to $m/z = 43$: ethylenimine ($\text{c-C}_2\text{H}_4\text{NH}$) and *N*-methylmethanimine (CH_3NCH_2). The maximum of the ion counts measured at $m/z = 43$ and $m/z = 42$ at 320 K correlates very well, suggesting that some of the ion counts measured at $m/z = 42$ could be due to fragmentation of $\text{C}_2\text{H}_5\text{N}^+$. Photofragmentation of ethylenimine ($\text{c-C}_2\text{H}_4\text{NH}$) into $\text{C}_2\text{H}_4\text{N}^+$ has been observed

by Gallegos and Kiser at 12.2 eV.⁸⁵ Therefore, it is highly likely that some of the ion counts observed at $m/z = 42$ are due to fragmentation of $c\text{-C}_2\text{H}_4\text{NH}^+$ ($m/z = 43$) to $c\text{-C}_2\text{H}_4\text{N}^+$. Ion counts at $m/z = 45$ can be assigned to isomers of molecular formula CH_3NO : nitrosomethane (CH_3NO), formamide (HCONH_2), and formaldehyde oxime (H_2CNOH). The TPD profile measured at $m/z = 45$ shows two maxima, which correlate well with the maxima observed in the TPD profile of $m/z = 30$, at around 280 and 320 K. This implies that ion signal at $m/z = 30$ at around 280 and 320 K could be due to NO^+ ions generated as a result of photofragmentation of nitrosomethane.⁸⁶ Therefore, we can conclude that some of the ion counts at $m/z = 45$ and $m/z = 30$ are due to the nitrosomethane ion (CH_3NO^+) and its fragment NO^+ , respectively. Finally, ion signal at $m/z = 46$ can be assigned to NO_2 (IE = 8.80 eV). Fragmentation of $m/z = 46$ (NO_2^+) to $m/z = 30$ (NO^+) can be easily presumed based on the fact that the TPD profile measured at $m/z = 46$ in the temperature range of 160–240 K is very similar to that of measured at $m/z = 30$. Dibeler et al. have demonstrated photofragmentation of nitrogen dioxide into NO^+ at 12.34 eV.⁸⁷ All three m/z values of 43, 45, and 46 have been reported previously in various experimental studies investigating the decomposition of RDX.^{4,9,28,34}

The TPD profiles of $m/z = 56, 58, 60, 70, 71$, and 72 are shown in Figure 6b. $m/z = 56$ was identified by Dickinson et al. and Zhao et al. while investigating the decomposition of RDX in the solid state and in the gas phase, respectively.^{9,34} $m/z = 56$ can be associated with the molecular formula $\text{C}_2\text{H}_4\text{N}_2$ (Table 4). Ion signal at $m/z = 58$ can be either allocated to the mononitroso form of methylene nitramine (H_2CNNO_2) holding the molecular structure H_2CNNO or to a primary amine moiety with the molecular formula $\text{C}_2\text{H}_6\text{N}_2$ (Table 4). Evidence of mass 58 has been reported earlier by Behrens and co-workers in thermal decomposition of RDX crystals.^{4,24} Decomposition product at $m/z = 60$ can be accounted for as the hydrogenated form of $m/z = 58$ (H_2CNNO and/or $\text{C}_2\text{H}_6\text{N}_2$) and hence might be assigned to the molecular formula $\text{CH}_4\text{N}_2\text{O}$ and/or $\text{C}_2\text{H}_8\text{N}_2$. Unlike $m/z = 56$ and 58 , evidence of $m/z = 60$ has not been reported in the previous studies. The ion signal at $m/z = 70, 71$, and 72 is linked to the molecular formulae $\text{C}_3\text{H}_6\text{N}_2$, $\text{C}_2\text{H}_5\text{N}_3$, and $\text{C}_3\text{H}_8\text{N}_2$, respectively (Table 4). The peak of the sublimation event of $m/z = 72$ at 320 K matches the maximum of the TPD profile at $m/z = 71$. Therefore, at least some ion counts at $m/z = 71$ likely represent fragments of $\text{C}_3\text{H}_8\text{N}_2^+$ ($m/z = 72$): $\text{C}_3\text{H}_7\text{N}_2^+$ ($m/z = 71$).

Figure 6c shows TPD profiles recorded at $m/z = 73, 74, 75, 81, 82$, and 83 . Like $m/z = 71$ ($\text{C}_2\text{H}_5\text{N}_3$), ion signal at $m/z = 73$ can be associated to an amine moiety. In fact, $m/z = 73$ can be designated to the hydrogenated counterpart of $\text{C}_2\text{H}_5\text{N}_3$ ($m/z = 71$) and, therefore, might be assigned to the molecular formula $\text{C}_2\text{H}_7\text{N}_3$ (Table 4). Similarly, $m/z = 75$ is attributed to the molecular formula $\text{C}_2\text{H}_9\text{N}_3$ because it might represent the hydrogenated analog of $m/z = 73$ ($\text{C}_2\text{H}_5\text{N}_3$) and/or 71 ($\text{C}_2\text{H}_5\text{N}_3$). It is important to mention that formation of higher molecular weight amine-based species have been predicted by ab initio molecular dynamics simulations, but these molecules have never been observed in experiments so far.¹⁶ In this study, both mass and FTIR spectra (Section 3.1) reveal evidence of formation of amines in the decomposition of RDX. Ion signal at $m/z = 74$ has been observed in several experimental studies and can be allocated to methylene nitramine (H_2CNNO_2),

formally the monomeric unit of RDX.⁹ Interestingly, TPD profiles measured at $m/z = 73, 74$, and 75 show peak maximum at the same temperature, 300 K. This could be either due to cosublimation of the products associated with $m/z = 73, 74$, and 75 or fragmentation of one species into another. Photofragmentation of $\text{C}_2\text{H}_9\text{N}_3$ ($m/z = 75$) to $\text{C}_2\text{H}_7\text{N}_3^+$ ($m/z = 73$) is highly viable. Similarly, the fragment of $\text{C}_2\text{H}_7\text{N}_3^+$ ($m/z = 73$)— $\text{C}_2\text{H}_6\text{N}_3^+$ —could contribute to the ion counts at $m/z = 72$.

Furthermore, ion signals at $m/z = 81, 82$, and 83 are assigned to the molecular formulae $\text{C}_3\text{H}_3\text{N}_3$, $\text{C}_3\text{H}_4\text{N}_3$, and $\text{C}_3\text{H}_5\text{N}_3$, respectively. These intermediates carry ring moieties of RDX and have been detected in the gas phase as well as condensed phase decomposition of RDX.^{8,34} The fragment of $\text{C}_3\text{H}_5\text{N}_3$ ($m/z = 83$)— $\text{C}_3\text{H}_4\text{N}_3^+$ —could account for the ion counts measured at $m/z = 82$. Higher masses carrying the ring moiety such as $m/z = 85$ and 87 are also observed in our experiments, and their TPD profiles are shown in Figure 6d. It is intriguing to note here that $m/z = 85$ and 87 have not been identified in previous studies. Figure 6d further shows TPD profiles of $m/z = 89, 91$, and 97 . Ion signal at $m/z = 89$ and 91 can be assigned to the molecular formulae $\text{CH}_3\text{N}_3\text{O}_2$ (aminomethylenenitramine) and $\text{CH}_5\text{N}_3\text{O}_2$ (aminomethylnitramine), respectively. Both molecules with likely structures presented in Table 4 have not been detected before.

The maximum of the ion counts measured at $m/z = 89$ and 91 appears at the same temperature of 300 K, suggesting that some of the ion counts at $m/z = 89$ arise from fragmentation of $\text{CH}_5\text{N}_3\text{O}_2^+$ ($m/z = 91$) into $\text{CH}_3\text{N}_3\text{O}_2^+$ ($m/z = 89$). Signal at $m/z = 97$ is associated to OST with the molecular formula $\text{C}_3\text{H}_3\text{N}_3\text{O}$. Until now, evidence of OST has been observed only during thermal decomposition of RDX in the liquid phase.^{4,24}

The plots of ion signal intensities as a function of temperature at higher mass-to-charge ratios of $m/z = 100, 101, 103, 105, 116, 117$, and 118 are compiled in Figure 6e. Interestingly, the ion signal intensities of these TPD profiles are nearly identical in low-dose and high-dose irradiation experiments. Ion signal at $m/z = 100$ has the same m/z as the mononitroso intermediate holding the molecular formula $\text{C}_2\text{H}_4\text{N}_4\text{O}$. The TPD profile at $m/z = 100$ and $m/z = 98$ are very similar suggesting that some of the ion counts at $m/z = 98$ are fragments of $m/z = 100$ ($\text{C}_2\text{H}_4\text{N}_4\text{O}^+$)— $\text{C}_2\text{H}_2\text{N}_4\text{O}^+$. Ion counts at $m/z 101, 103$, and 105 are likely associated to mononitro species with the molecular formulae $\text{C}_2\text{H}_3\text{N}_3\text{O}_2$, $\text{C}_2\text{H}_5\text{N}_3\text{O}_2$, and $\text{C}_2\text{H}_7\text{N}_3\text{O}_2$, respectively. It is intriguing to note here that fragmentation of $\text{C}_2\text{H}_5\text{N}_3\text{O}_2^+$ ($m/z = 103$) into $\text{C}_2\text{H}_3\text{N}_3\text{O}_2^+$ ($m/z 101$) is highly feasible. Although these mononitro species have not been identified in previous experimental studies, formation of the $\text{C}_2\text{H}_5\text{N}_3\text{O}_2$ and $\text{C}_2\text{H}_3\text{N}_3\text{O}_2$ radicals have been predicted by theoretical calculations.¹⁶ The ion signals at $m/z 116, 117$, and 118 are proposed to be associated with mononitro intermediates with the possible molecular formulae $\text{C}_2\text{H}_4\text{N}_4\text{O}_2$, $\text{C}_3\text{H}_7\text{N}_3\text{O}_2$, and $\text{C}_2\text{H}_6\text{N}_4\text{O}_2$, respectively. Ion counts at $m/z = 116$ could be due to fragmentation of $\text{C}_2\text{H}_6\text{N}_4\text{O}_2^+$ ($m/z = 118$) into $\text{C}_2\text{H}_4\text{N}_4\text{O}_2^+$ because the TPD profile recorded at $m/z = 116$ peaking at 280 and 320 K correlates well with two of the ion count maxima observed at 280 and 320 K in the sublimation profile measured at $m/z = 118$. Evidence of these species ($m/z = 116, 117, 118$) has not been reported through previous experimental or theoretical calculations.

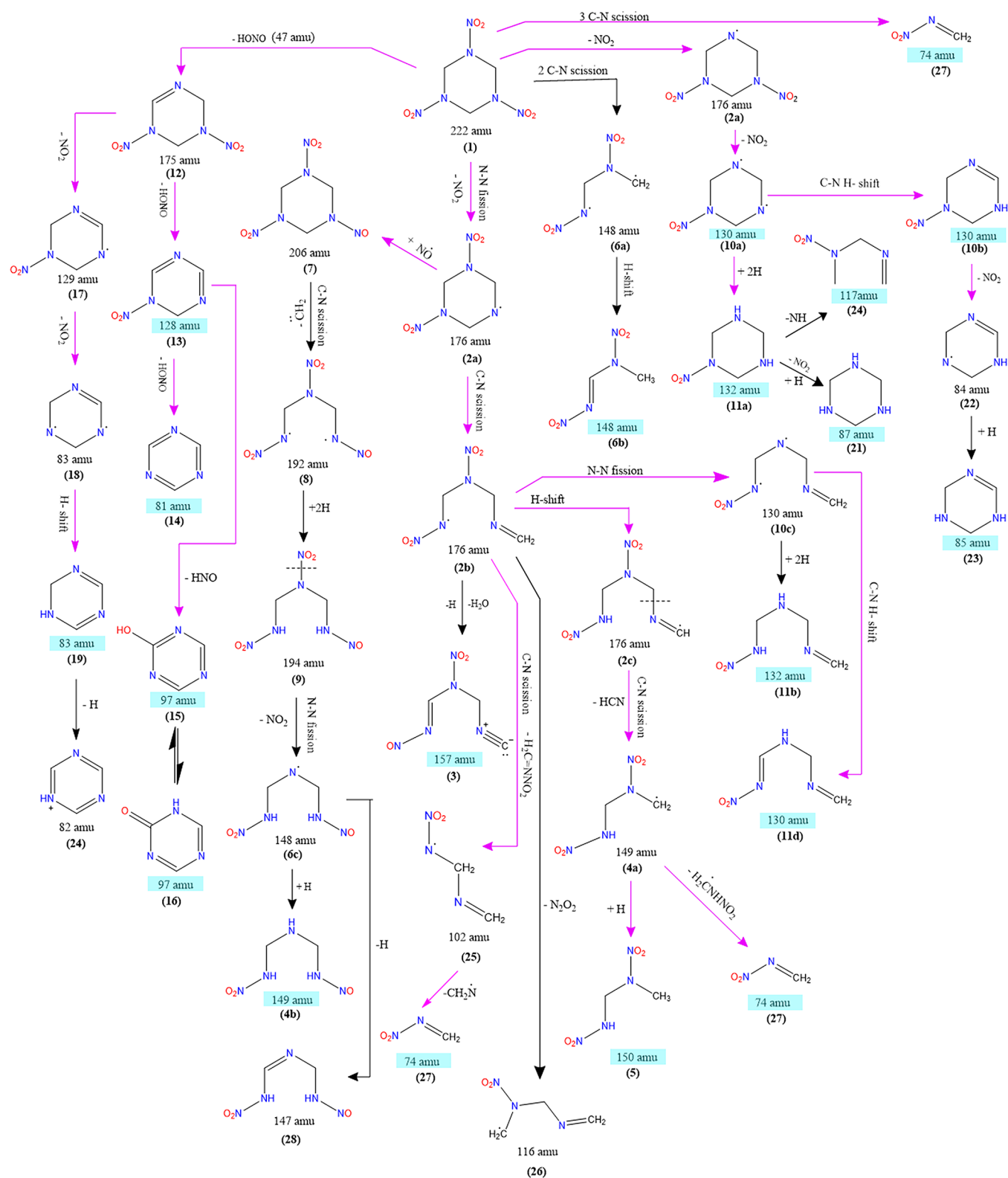


Figure 7. continued

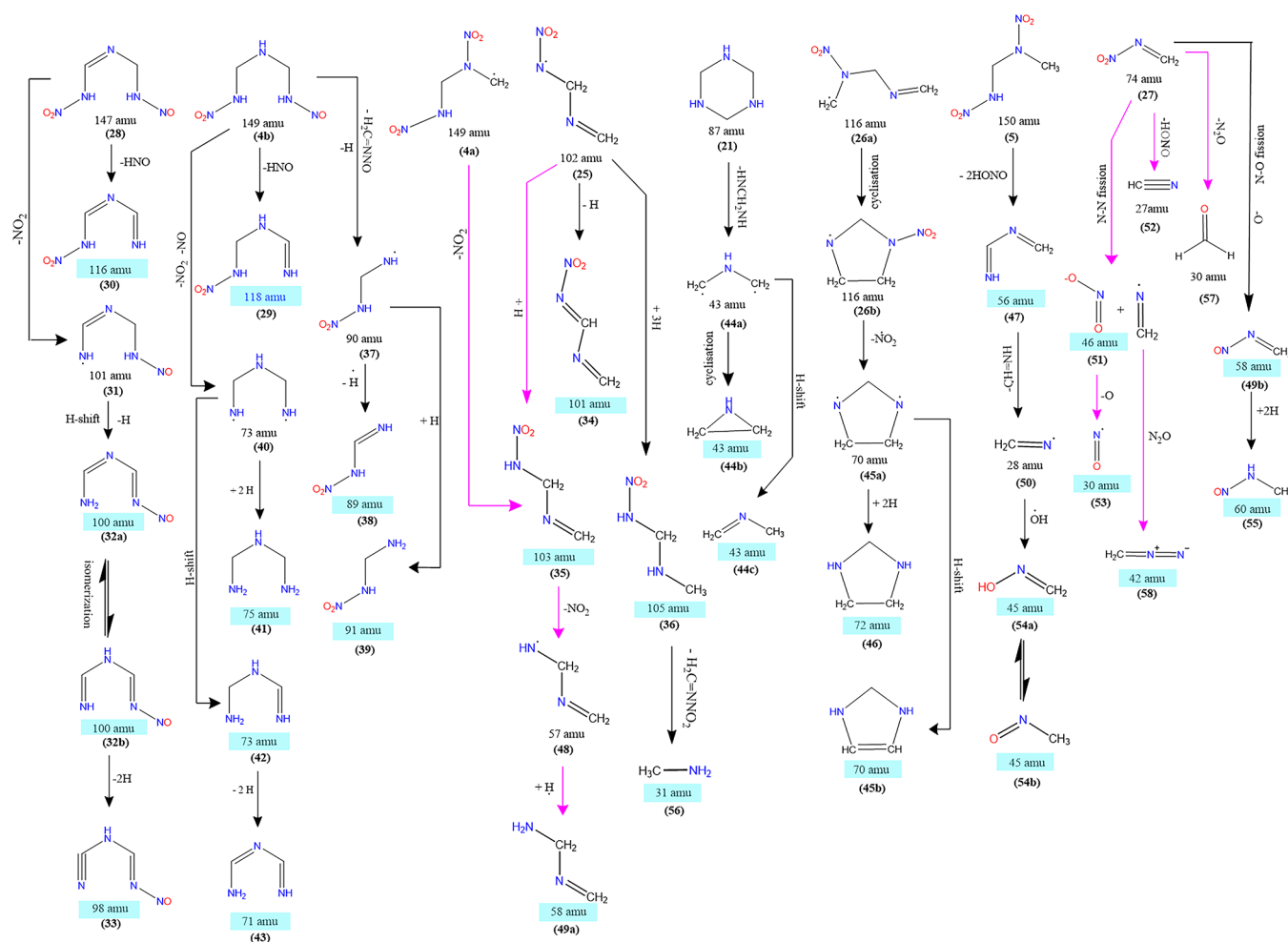


Figure 7. (a) Proposed decomposition mechanism of RDX into products at 157, 150, 149, 148, 132, 130, 128, 117, 97, 87, 85, 83, and 74 amu. Reaction mechanisms predicted by theoretical calculations are color coded in pink.^{14,16,18,22} (b) Proposed decomposition mechanism of RDX into products at 118, 116, 105, 103, 101, 100, 98, 91, 89, 75, 73, 72, 71, 70, 60, 58, 56, 46, 45, 43, 42, 31, and 30 amu. Reaction mechanisms predicted by theoretical calculations are color coded in pink.^{14,16,18}

Finally, TPD profiles of $m/z = 128$, 130, 132, 148, 149, 150, and 157 are shown in Figure 6f. Ion counts are higher by around 2 times in the low dose relative to high dose irradiation experiments. Signal at $m/z = 128$ is allocated to molecular formula $C_3H_4N_4O_2$ whose structure consists of the ring moiety of RDX with only one nitro group (Table 4 for structure). $m/z = 128$ has the highest signal intensity compared to all remaining masses in the low-dose irradiation experiment. Ion signal at $m/z = 130$ can be considered as hydrogenated form of $m/z = 128$ and hence might be assigned to $C_3H_6N_4O_2$. Evidence of formation of $m/z = 130$ has not been shown in previous experimental studies, but gas phase theoretical calculations predict its existence.¹⁶ Similarly, $m/z = 132$ could be designated as hydrogenated form of $m/z = 130$; its formation has been suggested by both experiments as well as theoretical calculations.^{4,9,16,24} On the basis of the similarity between the TPD profiles measured at $m/z = 130$ and 128, it can be envisaged that $C_3H_6N_4O_2^+$ ($m/z = 130$) could fragment into $C_3H_4N_4O_2^+$ ($m/z = 128$). Dinitro intermediates of RDX such as $m/z = 148$ and 150 are also observed in our experiment and are allocated to molecular formulae $C_2H_4N_4O_4$ and $C_2H_6N_4O_4$, respectively (Table 4). Signal at $m/z = 150$ can be considered as a hydrogenated form of $m/z = 148$; only the latter was detected during thermal decomposition of

RDX.^{9,14,16} We have also observed intermediates belonging to nitro–nitroso species, that is species carrying both a nitro and nitroso group via at $m/z = 149$ and 157. These species are assigned to molecular formulae $C_2H_7N_5O_3$ and $C_3H_3N_5O_3$, respectively. This is the first experimental evidence of formation of intermediates having both nitro and nitroso groups during the decomposition of RDX.

In summary, our ReTOF mass spectroscopic studies revealed several new decomposition products of RDX that have not been reported before. These include HNO ($m/z = 31$), CH_3N_2 ($m/z = 31$), CH_4N_2O ($m/z = 60$), $C_2H_5N_3$ ($m/z = 71$), $C_3H_8N_2$ ($m/z = 72$), $C_2H_9N_3$ ($m/z = 75$), $C_3H_7N_3$ ($m/z = 85$), $C_3H_9N_3$ ($m/z = 87$), $CH_3N_3O_2$ ($m/z = 89$), $CH_5N_3O_2$ ($m/z = 91$), $C_2H_2N_4O$ ($m/z = 98$), $C_2H_4N_4O$ ($m/z = 100$), $C_2H_3N_3O_2$ ($m/z = 101$), $C_2H_5N_3O_2$ ($m/z = 103$), $C_2H_7N_3O_2$ ($m/z = 105$), $C_2H_4N_4O_2$ ($m/z = 116$), $C_3H_7N_3O_2$ ($m/z = 117$), $C_2H_6N_4O_2$ ($m/z = 118$), $C_3H_6N_4O_2$ ($m/z = 130$), $C_2H_7N_5O_3$ ($m/z = 149$), $C_2H_6N_4O_4$ ($m/z = 150$), and $C_3H_3N_5O_3$ ($m/z = 157$). We observed intermediates that belong to amines, mononitro, and mononitroso families as well as intermediates that carry both nitro and nitroso groups. The underlying decomposition reactions involved in the formation of the observed species are proposed in the next section.

3.4. Decomposition Mechanism. Here, we discuss the decomposition pathways of RDX based on the reaction mechanisms proposed through gas-phase and condensed phase calculations accounting for the aforementioned experimental findings. The majority of the gas-phase calculations predict that the decomposition of RDX proceeds via N–NO₂ homolytic bond fission and/or 1,2-elimination of HONO; these pathways are suggested to be more favorable compared to alternative mechanisms such as concerted triple scission of C–N bonds forming H₂CNNO₂ and nitro–nitrite isomerization from N–NO₂ to N–ONO. The calculated energy barrier for the N–N fission (163 kJ mol^{−1}) and HONO elimination (164 kJ mol^{−1}) are significantly lower than the triple C–N scission (248 kJ mol^{−1}) or nitro–nitrite isomerization (192 kJ mol^{−1}).¹⁴ Condensed phase calculations also support N–N fission and HONO elimination as the primary steps in the decomposition of RDX.^{25,35–37} However, Monte Carlo variational transition-state theory calculations performed by Shalashilin and Thompson reveal that in gas phase thermal decomposition concerted triple C–N bond scission of RDX is more dominant compared to N–NO₂ bond fission.²⁰ On the basis of these mechanisms, we have presented a decomposition scheme of RDX in Figure 7a,b that reveals probable reactions involved in the formation of various decomposition products. These products can be broadly categorized into six species: dinitro, mononitro, mononitroso, nitro–nitroso, ring compounds, and smaller molecules.

3.4.1. Formation of Dinitro Species. At the early stage of RDX decomposition, the major products to be formed are dinitro species. Initially, the N–NO₂ fission of RDX (1) leads to a cyclic aminyl radical, **2a** (C₃H₆N₅O₄[•]); this process requires an energy of 163 kJ mol^{−1}.¹⁴ Radical **2a** can undergo a ring-opening reaction via C–N scission to form an acyclic isomer, **2b** (C₃H₆N₅O₄[•]) via a barrier of 110 kJ mol^{−1}.¹⁴ Intermediate **2b** (C₃H₆N₅O₄[•]) can further undergo a hydrogen-shift requiring 36 kJ mol^{−1}; this process forms yet another acyclic isomer with a carbon centered radical, **2c** (C₃H₆N₅O₄[•]).¹⁴ The intermediate **2c** decomposes to generate the carbon-centered radical, **4a** (C₂H₅N₄O₄[•]) along with a hydrogen cyanide (HCN) molecule via C–N β-scission. This reaction has a barrier of 68 kJ mol^{−1}.¹⁴ Addition of a hydrogen atom to **4a** results in a stable neutral intermediate, **5** (C₂H₆N₄O₄; 150 amu), which has been observed in our experiment. Alternatively, radical **4a** may encounter C–N scission to form methylene nitramine, **27** (CH₂NNO₂; 74 amu) and the CH₂NHNO₂[•] radical.¹⁴ The dinitro intermediate **6b** (C₂H₄N₄O₄; 148 amu) can form from RDX via 2 C–N scissions followed by a hydrogen atom shift. As mentioned before, the decomposition of RDX could also be initiated by concerted HONO elimination. The first HONO elimination from RDX leads to the dinitro intermediate, **12** (C₃H₅N₅O₄; 175 amu). The reaction barrier for HONO elimination (164 kJ mol^{−1}) is very similar to that of N–NO₂ fission.¹⁴

3.4.2. Formation of Mono-Nitro Species. The dinitro species formed during the early stage of decomposition can subsequently undergo C–N scission, N–N fission, or hydrogen atom shift to form mononitro species. For example, RDX (1) undergoes first a N–NO₂ fission to the dinitro radical, **2a** (C₃H₆N₅O₄[•]), which can subsequently undergo a second N–NO₂ fission to a cyclic biradical intermediate, **10a** (C₃H₆N₃O^{••}). This radical, **10a** undergoes hydrogen atom shift to form a cyclic mononitro, **10b** (C₃H₆N₄O₂; 130 amu), product. This process has a barrier of 187 kJ mol^{−1}.¹⁴

Intermediate **10a** can also accept two hydrogen atoms yielding a cyclic product, **11a** (C₃H₈N₄O₂; 132 amu). Both products (**10b** and **11a**) have been observed in our experiment. Product **11a** can further decompose to **24** (C₃H₇N₃O₂; 117 amu) via C–N scission and a hydrogen atom shift. Similarly, the acyclic aminyl radical **2b** (C₃H₆N₅O₄[•]) can form a biradical intermediate, **10c** (C₃H₆N₄O₂^{••}) via N–N fission which undergoes 1,2-H-shift to form an open chain isomer, **10d** (C₃H₆N₄O₂; 130 amu) of cyclic product, **10b**; this requires an energy of 190 kJ mol^{−1}.¹⁶ The biradical intermediate, **10c** can also accept two hydrogen radicals to form an acyclic isomer, **11b** (C₃H₈N₄O₂; 132 amu) of product **11a**. The acyclic aminyl radical, **2b** (C₃H₆N₅O₄[•]) can also experience a C–N scission, which requires 103 kJ mol^{−1} of energy to form a mononitro N-centered radical, **25** (C₂H₄N₃O₂[•]) and methylene nitramine **27** (CH₂NNO₂; 74 amu).¹⁴ The radical **25** could engage in C–N scission to form a molecule of methylene nitramine (CH₂NNO₂; 74 amu) and H₂CN; this process requires an additional energy of 84 kJ mol^{−1} relative to that of radical **25** (C₂H₄N₃O₂[•]). Alternatively, radical **25** can react further by either abstracting a hydrogen atom to form the mononitro product, **35** (C₂H₅N₃O₂; 103 amu) or by eliminating a hydrogen atom to yield product **34** (C₂H₃N₃O₂; 101 amu) (Figure 7b). Furthermore, the addition of three hydrogen atoms to radical **25** can generate product **36** (C₂H₇N₃O₂; 105 amu; Figure 7b).¹⁴ Interestingly, all four mononitro products (103, 101, 105, and 74 amu) have been observed in our experiment. The acyclic aminyl radical, **2b** (C₃H₆N₅O₄[•]) can also decompose to a mononitro carbon centered radical, **26** (C₃H₆N₃O₂[•]) via elimination of N₂O₂ (Figure 7a). Radical **26** (C₃H₆N₃O₂[•]) may involve in the formation of five membered ring species, which will be discussed later. The dinitro intermediate, **12** (C₃H₅N₅O₄; 175 amu) formed via concerted HONO elimination from RDX can eliminate yet another HONO molecule to the mononitro product, **13** (C₃H₄N₃O₂; 128 amu) (Figure 7a) with a barrier of 134 kJ mol^{−1}.¹⁴ Intermediate **13** undergoes decomposition to form various cyclic species which will be discussed later.

3.4.3. Formation of Ring Compounds. Species carrying the cyclic RDX moiety mainly originate from cyclic dinitro or mononitro compounds formed via HONO elimination or N–NO₂ fission(s). The most common cyclic product is triazine **14** (C₃H₃N₃; 81 amu), which is formed via HONO elimination from the mononitro intermediate, **13** (C₃H₄N₃O₂; 128 amu). The calculated energy barrier for this reaction is 84 kJ mol^{−1}.¹⁴ Besides triazine, our experiments also suggest the formation of oxy-sym-triazine (OST) **15** (C₃H₃N₃O; 97 amu). Formation of this molecule has been proposed computationally from the mononitro intermediate, **13** (C₃H₄N₃O₂; 128 amu) after elimination of a HNO molecule.^{3,14} Hydrogenated forms of the triazine ring such as C₃H₅N₃ (83 amu), C₃H₇N₃ (85 amu), and C₃H₉N₃ (87 amu) could be generated from mononitro intermediates via successive N–NO₂ fission reactions. For example, the dinitro intermediate, **12** (C₃H₅N₅O₄; 175 amu), which is formed via HONO elimination from RDX, could undergo two successive N–NO₂ fission reactions to form a nitrogen-centered biradical, **18** (C₃H₅N₃^{••}). The energy required for this process is around 184 kJ mol^{−1}.¹⁶ Radical **18** can further undergo a hydrogen shift, yielding **19** (C₃H₅N₃; 83 amu). Similarly, **23** (C₃H₇N₃; 85 amu) can originate from the mononitro species, **10b** via N–NO₂ fission followed by a hydrogen atom addition. The fully hydrogenated form of triazine (C₃H₉N₃; 87 amu) can be formed from mononitro

11a ($\text{C}_3\text{H}_8\text{N}_4\text{O}_2$; 132 amu) after N–NO₂ fission followed by hydrogen addition. Five membered ring species such as $\text{C}_3\text{H}_8\text{N}_2$ (72 amu) and $\text{C}_3\text{H}_6\text{N}_2$ (70 amu) are also observed. These products could originate from a mononitro radical, 26 ($\text{C}_3\text{H}_6\text{N}_3\text{O}_2^\bullet$) via the ring closure mechanism (Figure 7b). Cyclization of radical 26 leads to a cyclic nitrogen-centered radical, which can undergo hydrogen addition followed by N–N fission to form another nitrogen-centered radical, 45a ($\text{C}_3\text{H}_6\text{N}_2^\bullet$). This radical (45) can abstract a hydrogen to form product 46 ($\text{C}_3\text{H}_8\text{N}_2$; 72 amu) or it may release a hydrogen atom to form 45b ($\text{C}_3\text{H}_6\text{N}_2$; 70 amu).

3.4.4. Formation of Nitro–Nitroso Species. Products carrying both a nitro and nitroso groups have not been observed before with the exception of ONDNNTA (7).⁴ Here, we see few products that could originate from ONDNNTA. It has been suggested that the ONDNNTA is formed via recombination of cyclic aminyl radical 2a ($\text{C}_3\text{H}_6\text{N}_5\text{O}_4^\bullet$) with nitrogen monoxide (NO) at the early stage of decomposition.^{5,22} ONDNNTA (7) eventually undergoes C–N scission to form an acyclic nitrogen-centered biradical, 8 ($\text{C}_2\text{H}_4\text{N}_6\text{O}_5^{\bullet\bullet}$). Radical 8 can accept two hydrogens to form 9 ($\text{C}_2\text{H}_6\text{N}_6\text{O}_5$; 194 amu); the latter may undergo N–N fission leading to a nitrogen-centered radical, 6c ($\text{C}_2\text{H}_6\text{N}_5\text{O}_3^\bullet$). Addition of a hydrogen atom to radical 6c gives rise to an intermediate, 4b ($\text{C}_2\text{H}_7\text{N}_5\text{O}_3$; 149 amu). Alternately, a hydrogen atom can be abstracted from 6c to produce intermediate 28 ($\text{C}_2\text{H}_5\text{N}_5\text{O}_3$; 147 amu). Intermediate 4b can further dissociate to form the mononitro product 29 ($\text{C}_2\text{H}_6\text{N}_4\text{O}_2$; 118 amu) via elimination of a HNO molecule (Figure 7b). Similarly, intermediate 28 may eliminate a HNO molecule to form the mononitro product 30 ($\text{C}_2\text{H}_4\text{N}_4\text{O}_2$; 116 amu; Figure 7b). Intermediate 4b ($\text{C}_2\text{H}_7\text{N}_5\text{O}_3$; 149 amu) can also lead to a nitrogen-centered radical 37 ($\text{CH}_4\text{N}_3\text{O}_2^\bullet$) via elimination of a nitrosoamine radical ($\text{CH}_2\text{NHNO}^\bullet$). The reactive radical 37 eventually either abstracts a hydrogen atom to form 39 ($\text{CH}_5\text{N}_3\text{O}_2$; 91 amu) or releases a hydrogen atom yielding 38 ($\text{CH}_3\text{N}_3\text{O}_2$; 89 amu). The nitro–nitroso intermediates such as 3 ($\text{C}_3\text{H}_3\text{N}_5\text{O}_3$; 157 amu) can be generated from a cyclic aminyl radical, 2b ($\text{C}_3\text{H}_6\text{N}_5\text{O}_4^\bullet$) after eliminating water and a hydrogen atom (Figure 7a).

3.4.5. Formation of Mono-Nitroso Species. Products carrying both nitro and nitroso groups could represent the precursor for mononitroso species. For example, the mononitroso product, 32a ($\text{C}_2\text{H}_4\text{N}_4\text{O}$; 100 amu) may form from intermediate 28 ($\text{C}_2\text{H}_6\text{N}_5\text{O}_3$; 147 amu) after elimination of nitrogen dioxide followed by hydrogen atom shift (Figure 7b). Hydrogen abstraction from molecule 32a could lead to product 33 ($\text{C}_2\text{H}_2\text{N}_4\text{O}$; 98 amu).

3.4.6. Formation of Amines. Mononitro and nitro–nitroso species can decompose into amines via N–NO₂ fission as well as C–N scission mechanisms (Figure 7b). For example, mononitro product 35 ($\text{C}_2\text{H}_5\text{N}_3\text{O}_2$; 103 amu) can undergo N–NO₂ fission to form a nitrogen-centered amine radical, 48 ($\text{C}_2\text{H}_5\text{N}_2^\bullet$), which can accept a hydrogen atom to generate an amine product, 49a ($\text{C}_2\text{H}_6\text{N}_2$; 58 amu). The barrier to this process is about 189 kJ mol^{−1}. Likewise, intermediate 4b can decompose into diamine radical 40 via two successive N–N fission reactions; this radical can then undergo a hydrogen-shift to generate 42 ($\text{C}_2\text{H}_7\text{N}_3$; 73 amu). Alternatively, radical 40 may accept two hydrogen atoms to form the diamine, 41 ($\text{C}_2\text{H}_9\text{N}_3$; 75 amu). Species 42 can further release two hydrogen atoms to produce 43 ($\text{C}_2\text{H}_5\text{N}_3$; 71 amu). Mononitro 36 can decompose into a molecule of methylene nitramine

plus methylamine (CH_3NH_2 ; 31 amu; 56) via C–N scission. Ring compounds such as 21 ($\text{C}_3\text{H}_9\text{N}_3$; 87 amu) can also decompose to generate a carbon-centered biradical 44a ($\text{C}_2\text{H}_5\text{N}^{\bullet\bullet}$). Radical 44a can either undergo ring closure to 44b ($\text{c-C}_2\text{H}_5\text{N}$; 43 amu) or hydrogen-shift to 44c ($\text{C}_2\text{H}_5\text{N}$; 43 amu). Dinitro species 5 can undergo two successive HONO eliminations to generate 47 ($\text{C}_2\text{H}_4\text{N}_2$; 56 amu).

3.4.7. Formation of Small Molecules. Finally, methylene nitramine 27 (CH_2NNO_2 ; 74 amu) formed from higher molecular weight species decomposes into secondary products such as dinitrogen oxide (N_2O), hydrogen cyanide (HCN), nitrogen monoxide (NO; 30 amu; 53), formaldehyde (H_2CO ; 30 amu; 52), and methylene nitrosoamine (CH_2NNO ; 58 amu; 49b). Several pathways for the decomposition of methylene nitramine exist. (i) The N–NO₂ fission of 27 (CH_2NNO_2 ; 74 amu) results in formation of NO₂ (46 amu; 51) and $\text{CH}_2\text{N}^\bullet$ (28 amu; 50) radical. (ii) Methylene nitramine, 27 (CH_2NNO_2 ; 74 amu) can also undergo HONO elimination to form hydrogen cyanide (HCN) (27 amu; 52). (iii) It can also decompose into dinitrogen oxide (N_2O) and formaldehyde (H_2CO ; 30 amu; 57). (iv) Another possibility is the N–O fission, which results in the formation of methylene nitrosoamine (CH_2NNO ; 58 amu; 49b). Product 49b can undergo hydrogen addition to form methyl nitrosoamine (CH_3NHNO ; 60 amu; 55). The $\text{CH}_2\text{N}^\bullet$ radical, 50 formed from methylene nitramine via N–NO₂ fission can combine with $^\bullet\text{OH}$ radical to form formaldoxime (CH_2NOH ; 45 amu; 54a), which can isomerize to nitroso methane (CH_3NO ; 45 amu; 54b).

4. CONCLUSIONS

In the present study, the decomposition of RDX by energetic electrons was explored using a surface science machine at 5 K. The decomposition products were probed by exploiting the FTIR, UV–vis, and Re-TOF-PI techniques. Our FTIR data revealed the formation of simple decomposition products such as water (H_2O), carbon dioxide (CO_2), dinitrogen oxide (N_2O), hydrogen cyanide (HCN), nitrogen monoxide (NO), formaldehyde (H_2CO), nitrous acid (HONO), and nitrogen dioxide (NO_2). 38 species were detected through ReTOF-PI mass spectroscopy at m/z values from 39 to 157. Products observed at m/z values of 31, 60, 71, 72, 75, 85, 87, 89, 91, 98, 100, 101, 103, 105, 116, 117, 118, 130, 149, 150, and 157 were detected for the first time. The new products observed in the present study belong to six classes. These are (i) dinitro compounds: $\text{C}_2\text{H}_6\text{N}_4\text{O}_4$ ($m/z = 150$), (ii) mononitro compounds: $\text{CH}_3\text{N}_3\text{O}_2$ ($m/z = 89$), $\text{CH}_5\text{N}_3\text{O}_2$ ($m/z = 91$), $\text{C}_2\text{H}_3\text{N}_3\text{O}_2$ ($m/z = 101$), $\text{C}_2\text{H}_5\text{N}_3\text{O}_2$ ($m/z = 103$), $\text{C}_2\text{H}_7\text{N}_3\text{O}_2$ ($m/z = 105$), $\text{C}_2\text{H}_6\text{N}_4\text{O}_2$ ($m/z = 118$), and $\text{C}_3\text{H}_6\text{N}_4\text{O}_2$ ($m/z = 130$); (iii) mononitroso compounds: $\text{CH}_4\text{N}_2\text{O}$ ($m/z = 60$), $\text{C}_2\text{H}_2\text{N}_4\text{O}$ ($m/z = 98$), and $\text{C}_2\text{H}_4\text{N}_4\text{O}$ ($m/z = 100$); (iv) nitro–nitroso compounds: $\text{C}_3\text{H}_3\text{N}_5\text{O}_3$ ($m/z = 157$) and $\text{C}_2\text{H}_7\text{N}_5\text{O}_3$ ($m/z = 149$), (v) cyclic compounds: $\text{C}_3\text{H}_8\text{N}_2$ ($m/z = 72$), $\text{C}_2\text{H}_6\text{N}_3$ ($m/z = 75$), $\text{C}_3\text{H}_7\text{N}_3$ ($m/z = 85$), and $\text{C}_3\text{H}_9\text{N}_3$ ($m/z = 87$), and (vi) amines: $\text{C}_2\text{H}_5\text{N}_3$ ($m/z = 71$) and $\text{C}_2\text{H}_9\text{N}_3$ ($m/z = 75$). We also inferred reactive radical intermediates such as $\text{c-C}_3\text{H}_6\text{N}_4\text{O}_2^\bullet$, $\text{C}_3\text{H}_6\text{N}_4\text{O}_2^\bullet$, $\text{C}_2\text{H}_5\text{N}_4\text{O}_4^\bullet$, $\text{C}_2\text{H}_4\text{N}_3\text{O}_2^\bullet$, $\text{c-C}_3\text{H}_5\text{N}_3^\bullet$, and $\text{C}_2\text{H}_5\text{N}_2^\bullet$; previously these radical species have only been predicted through electronic calculations. Finally, the decomposition mechanisms leading to the observed products have been discussed. Overall, the decomposition of RDX is most likely initiated via N–NO₂ fission that leads to the formation of a cyclic aminyl radical,

which can further undergo C–N scission, N–NO₂ fission, or hydrogen-shift to form dinitro and mononitro intermediates. Alternatively, RDX decomposes through HONO elimination to form dinitro, mononitro, and triazine-like cyclic compounds. Dinitro and mononitro products could further experience C–N scission or N–NO₂ fission to form methylene nitramine as well as amines. Methylene nitramine further fragments into secondary products such as dinitrogen oxide (N₂O), hydrogen cyanide (HCN), nitrogen monoxide (NO), formaldehyde (H₂CO), and nitrogen dioxide (NO₂). The mononitroso and nitro–nitroso species most likely originate from ONDNTA. The latter could form at an early stage of the decomposition via radical recombination of cyclic aminyl radical and nitrogen monoxide (NO). Mononitroso and nitro–nitroso species were detected, as well.

An investigation of the decomposition of RDX as conducted in the present experiments is very challenging and insights can be provided by merging the experimental results with a computational investigation of decomposition pathways. The present study represents the very first step in an investigation of the decomposition by ionizing radiation. Further experiments should exploit tunable VUV light to explicitly identify the nature of the decomposition products. This requires a computational determination of the ionization energies of all structural isomers. Finally, additional insights will be obtained by selectively photo exciting RDX under the same experimental conditions of 5 K via distinct transitions with the goal to selectively cleave—at least initially—N–NO₂, C–N, N–O, and C–H bonds.

■ ASSOCIATED CONTENT

● Supporting Information

The Supporting Information is available free of charge on the ACS Publications website at DOI: 10.1021/acs.jpca.9b08695.

NMR spectra and IR spectra (PDF)

■ AUTHOR INFORMATION

Corresponding Author

*E-mail: ralfk@hawaii.edu.

ORCID

Ralf I. Kaiser: 0000-0002-7233-7206

Notes

The authors declare no competing financial interest.

■ ACKNOWLEDGMENTS

This project was supported by the U.S. Army Research Office (ARO) (W911NF1810438).

■ REFERENCES

- (1) Adams, G. F.; Shaw, R. W. Chemical reactions in energetic materials. *Annu. Rev. Phys. Chem.* **1992**, *43*, 311–340.
- (2) *Chemistry of Energetic Materials*; Olah, D. S. G., Ed.; Academic Press: San Diego, 1991.
- (3) *Chemistry and Physics of Energetic Materials*; Bulusu, S. N., Ed.; Springer: Netherlands, 1990.
- (4) Behrens, R.; Bulusu, S. Thermal decomposition of energetic materials. 3. Temporal behaviors of the rates of formation of the gaseous pyrolysis products from condensed-phase decomposition of 1,3,5-trinitrohexahydro-s-triazine (RDX). *J. Phys. Chem.* **1992**, *96*, 8877–8891.
- (5) Behrens, R.; Bulusu, S. Thermal decomposition of energetic materials. 4. Deuterium isotope effects and isotopic scrambling (H/D, ¹³C/¹⁸O, ¹⁴N/¹⁵N) in condensed-phase decomposition of 1,3,5-trinitrohexahydro-s-triazine (RDX). *J. Phys. Chem.* **1992**, *96*, 8891–8897.
- (6) Greenfield, M.; Guo, Y. Q.; Bernstein, E. R. Ultrafast photodissociation dynamics of HMX and RDX from their excited electronic states via femtosecond laser pump–probe techniques. *Chem. Phys. Lett.* **2006**, *430*, 277–281.
- (7) Guo, Y. Q.; Greenfield, M.; Bhattacharya, A.; Bernstein, E. R. On the excited electronic state dissociation of nitramine energetic materials and model systems. *J. Chem. Phys.* **2007**, *127*, 154301.
- (8) Im, H.-S.; Bernstein, E. R. On the initial steps in the decomposition of energetic materials from excited electronic states. *J. Chem. Phys.* **2000**, *113*, 7911–7918.
- (9) Zhao, X.; Hints, E. J.; Lee, Y. T. Infrared multiphoton dissociation of RDX in a molecular beam. *J. Chem. Phys.* **1988**, *88*, 801–810.
- (10) Lemire, G. W.; Simeonsson, J. B.; Sausa, R. C. Monitoring of vapor-phase nitro compounds using 226-nm radiation: fragmentation with subsequent NO resonance-enhanced multiphoton ionization detection. *Anal. Chem.* **1993**, *65*, 529–533.
- (11) Zuckermann, H.; Greenblatt, G. D.; Haas, Y. Hydroxyl radical formation in the infrared multiphoton decomposition of jet-cooled cyclic nitroamines. *J. Phys. Chem.* **1987**, *91*, 5159–5161.
- (12) Wu, C. J.; Fried, L. E. Ab initio study of RDX decomposition mechanisms. *J. Phys. Chem. A* **1997**, *101*, 8675–8679.
- (13) Molt, R. W.; Watson, T.; Bazanté, A. P.; Bartlett, R. J.; Richards, N. G. J. Gas phase RDX decomposition pathways using coupled cluster theory. *Phys. Chem. Chem. Phys.* **2016**, *18*, 26069–26077.
- (14) Chakraborty, D.; Muller, R. P.; Dasgupta, S.; Goddard, W. A. The mechanism for unimolecular decomposition of RDX (1,3,5-Trinitro-1,3,5-triazine), an ab initio study. *J. Phys. Chem. A* **2000**, *104*, 2261–2272.
- (15) Swadley, M. J.; Li, T. Reaction mechanism of 1,3,5-trinitro-s-triazine (RDX) deciphered by density functional theory. *J. Chem. Theory Comput.* **2007**, *3*, 505–513.
- (16) Schweigert, I. V. Ab initio molecular dynamics of high-temperature unimolecular dissociation of gas-phase RDX and its dissociation products. *J. Phys. Chem. A* **2015**, *119*, 2747–2759.
- (17) Sharia, O.; Kuklja, M. M. Ab initio kinetics of gas phase decomposition reactions. *J. Phys. Chem. A* **2010**, *114*, 12656–12661.
- (18) Harris, N. J.; Lammertsma, K. Ab initio density functional computations of conformations and bond dissociation energies for hexahydro-1,3,5-trinitro-1,3,5-triazine. *J. Am. Chem. Soc.* **1997**, *119*, 6583–6589.
- (19) Bhattacharya, A.; Bernstein, E. R. Nonadiabatic decomposition of gas-phase RDX through conical intersections: an ONIOM-CASSCF study. *J. Phys. Chem. A* **2011**, *115*, 4135–4147.
- (20) Shalashilin, D. V.; Thompson, D. L. Monte carlo variational transition-state theory study of the unimolecular dissociation of RDX. *J. Phys. Chem. A* **1997**, *101*, 961–966.
- (21) Rice, B. M.; Adams, G. F.; Page, M.; Thompson, D. L. Classical dynamics simulations of unimolecular decomposition of CH₂NNO₂: HONO elimination vs N–N bond scission. *J. Phys. Chem.* **1995**, *99*, 5016–5028.
- (22) Irikura, K. K. Aminoxyl (Nitroxyl) radicals in the early decomposition of the nitramine RDX. *J. Phys. Chem. A* **2013**, *117*, 2233–2241.
- (23) Akin, F. A. Ionisation energy, electron affinity, and mass spectral decomposition mechanisms of RDX isomers upon electron attachment and electron ionisation. *Mol. Phys.* **2016**, *114*, 3556–3566.
- (24) Maharrey, S.; Behrens, R. Thermal decomposition of energetic materials. 5. Reaction processes of 1,3,5-trinitrohexahydro-s-triazine below its melting point. *J. Phys. Chem. A* **2005**, *109*, 11236–11249.
- (25) Miao, M.; Dreger, Z. A.; Patterson, J. E.; Gupta, Y. M. Shock wave induced decomposition of RDX: quantum chemistry calculations. *J. Phys. Chem. A* **2008**, *112*, 7383–7390.
- (26) Makarov, I. E.; Zhestkova, T. P.; Zhukova, T. N. Radiation-induced decomposition of cyclotrimethylenetrinitramine in aqueous solutions. *High Energy Chem.* **2011**, *45*, 89–92.

- (27) Botcher, T. R.; Wight, C. A. Transient thin film laser pyrolysis of RDX. *J. Phys. Chem.* **1993**, *97*, 9149–9153.
- (28) Lee, Y.; Tang, C.-J.; Litzinger, T. A. A study of the chemical and physical processes governing CO₂ laser-induced pyrolysis and combustion of RDX. *Combust. Flame* **1999**, *117*, 600–628.
- (29) Gongwer, P. E.; Brill, T. B. Thermal decomposition of energetic materials 73: the identity and temperature dependence of “minor” products from flash-heated RDX. *Combust. Flame* **1998**, *115*, 417–423.
- (30) Capellos, C.; Papagiannakopoulos, P.; Liang, Y.-L. The 248 nm photodecomposition of hexahydro-1,3,5-trinitro-1,3,5-triazine. *Chem. Phys. Lett.* **1989**, *164*, 533–538.
- (31) Tang, T. B.; Chaudhuri, M. M.; Rees, C. S.; Mullock, S. J. Decomposition of solid explosives by laser irradiation: a mass spectrometric study. *J. Mater. Sci.* **1987**, *22*, 1037–1044.
- (32) Dang, N. C.; Gottfried, J. L.; De Lucia, F. C. Energetic material response to ultrafast indirect laser heating. *Appl. Opt.* **2017**, *56*, B85–B91.
- (33) Gares, K. L.; Bykov, S. V.; Brinzer, T.; Asher, S. A. Solution and solid hexahydro-1,3,5-trinitro-1,3,5-triazine (RDX) ultraviolet (UV) 229 nm photochemistry. *Appl. Spectrosc.* **2015**, *69*, 545–554.
- (34) Dickinson, J. T.; Jensen, L. C.; Doering, D. L.; Yee, R. Mass spectroscopy study of products from exposure of cyclotrimethylene-trinitramine single crystals to KrF excimer laser radiation. *J. Appl. Phys.* **1990**, *67*, 3641–3651.
- (35) Čapková, P.; Pospíšil, M.; Vávra, P.; Zeman, S. Characterisation of explosive materials using molecular dynamics simulations. In *Theoretical and Computational Chemistry*; Politzer, P., Murray, J. S., Eds.; Elsevier, 2003; Vol. 12, pp 49–60.
- (36) Strachan, A.; Kober, E. M.; van Duin, A. C. T.; Ongaard, J. Thermal decomposition of RDX from reactive molecular dynamics. *J. Chem. Phys.* **2005**, *122*, 054502.
- (37) Goddard, K.; Losada, M.; Chaudhuri, S. Intermolecular energy transfer dynamics at a hot-spot interface in RDX crystals. *J. Phys. Chem. A* **2016**, *120*, 477–489.
- (38) Connor, L. E.; Morrison, C. A.; Oswald, I. D. H.; Pulham, C. R.; Warren, M. R. Carbon dioxide binary crystals via the thermal decomposition of RDX at high pressure. *Chem. Sci.* **2017**, *8*, 4872–4878.
- (39) Song, N.-M.; Yang, L.; Han, J.-M.; Liu, J.-C.; Zhang, G.-Y.; Gao, H.-X. Catalytic study on thermal decomposition of Cu-en/(AP, CL-20, RDX and HMX) composite microspheres prepared by spray drying. *New J. Chem.* **2018**, *42*, 19062–19069.
- (40) Wynn, C. M.; Palmacci, S.; Kunz, R. R.; Clow, K.; Rothschild, M. Detection of condensed-phase explosives via laser-induced vaporization, photodissociation, and resonant excitation. *Appl. Opt.* **2008**, *47*, 5767–5776.
- (41) Brill, T. B.; Beckstead, M. C.; Flanagan, J. E.; Lin, M. C.; Litzinger, T. A.; Woodward Waesche, R. H.; Wight, C. A. Chemical speciation and dynamics in the surface combustion zone of energetic materials. *J. Propul. Power* **2002**, *18*, 824–834.
- (42) Cosgrove, J. D.; Owen, A. J. The thermal decomposition of 1,3,5-trinitrohexahydro-1,3,5-triazine (RDX). *Chem. Commun.* **1968**, 286.
- (43) Rauch, F. C.; Fanelli, A. J. Thermal decomposition kinetics of hexahydro-1,3,5-trinitro-s-triazine above the melting point: evidence for both a gas and liquid phase decomposition. *J. Phys. Chem.* **1969**, *73*, 1604–1608.
- (44) Cosgrove, J. D.; Owen, A. J. The thermal decomposition of 1,3,5 trinitro hexahydro 1,3,5 triazine (RDX)—part I: the products and physical parameters. *Combust. Flame* **1974**, *22*, 13–18.
- (45) Cosgrove, J. D.; Owen, A. J. The thermal decomposition of 1,3,5 trinitro hexahydro 1,3,5 triazine (RDX)—part II: the effects of the products. *Combust. Flame* **1974**, *22*, 19–22.
- (46) Batten, J. The thermal decomposition of RDX at temperatures below the melting point. III. Towards the elucidation of the mechanism. *Aust. J. Chem.* **1971**, *24*, 945–954.
- (47) Batten, J. The thermal decomposition of RDX at temperatures below the melting point. IV. Catalysis of the decomposition by formaldehyde. *Aust. J. Chem.* **1971**, *24*, 2025–2029.
- (48) Góbi, S.; Crandall, P. B.; Maksyutenko, P.; Förstel, M.; Kaiser, R. I. Accessing the nitromethane (CH₃NO₂) potential energy surface in methanol (CH₃OH)–nitrogen monoxide (NO) ices exposed to ionizing radiation: an FTIR and PI-ReTOF-MS investigation. *J. Phys. Chem. A* **2018**, *122*, 2329–2343.
- (49) Kaiser, R. I.; Maksyutenko, P. Novel reaction mechanisms pathways in the electron induced decomposition of solid nitromethane (CH₃NO₂) and D3-nitromethane (CD₃NO₂). *J. Phys. Chem. C* **2015**, *119*, 14653–14668.
- (50) Kaiser, R. I.; Maksyutenko, P. A mechanistical study on non-equilibrium reaction pathways in solid nitromethane (CH₃NO₂) and D3-nitromethane (CD₃NO₂) upon interaction with ionizing radiation. *Chem. Phys. Lett.* **2015**, *631–632*, 59–65.
- (51) Maksyutenko, P.; Muzangwa, L. G.; Jones, B. M.; Kaiser, R. I. Lyman α photolysis of solid nitromethane (CH₃NO₂) and D3-nitromethane (CD₃NO₂) – untangling the reaction mechanisms involved in the decomposition of model energetic materials. *Phys. Chem. Chem. Phys.* **2015**, *17*, 7514–7527.
- (52) Bennett, C. J.; Brotton, S. J.; Jones, B. M.; Misra, A. K.; Sharma, S. K.; Kaiser, R. I. High-sensitivity raman spectrometer to study pristine and irradiated interstellar ice analogs. *Anal. Chem.* **2013**, *85*, 5659–5665.
- (53) Jones, B. M.; Kaiser, R. I. Application of reflectron time-of-flight mass spectroscopy in the analysis of astrophysically relevant ices exposed to ionization radiation: methane (CH₄) and D4-methane (CD₄) as a case study. *J. Phys. Chem. Lett.* **2013**, *4*, 1965–1971.
- (54) Bergantini, A.; Abplanalp, M. J.; Pokhilkov, P.; Krylov, A. I.; Shingledecker, C. N.; Herbst, E.; Kaiser, R. I. A combined experimental and theoretical study on the formation of interstellar propylene oxide (CH₃CHCH₂O)—a chiral molecule. *Astrophys. J.* **2018**, *860*, 108.
- (55) Isbell, R. A.; Brewster, M. Q. Optical properties of energetic materials: RDX, HMX, AP, NC/NG, and HTPB. *Propellants, Explos., Pyrotech.* **1998**, *23*, 218–224.
- (56) Drouin, D.; Couture, A. R.; Joly, D.; Tastet, X.; Aimez, V.; Gauvin, R. CASINO V2.42—a fast and easy-to-use modeling tool for scanning electron microscopy and microanalysis users. *Scanning* **2007**, *29*, 92–101.
- (57) Maity, S.; Kaiser, R. I.; Jones, B. M. Formation of complex organic molecules in methanol and methanol–carbon monoxide ices exposed to ionizing radiation – a combined FTIR and reflectron time-of-flight mass spectrometry study. *Phys. Chem. Chem. Phys.* **2015**, *17*, 3081–3114.
- (58) Abplanalp, M. J.; Jones, B. M.; Kaiser, R. I. Untangling the methane chemistry in interstellar and solar system ices toward ionizing radiation: a combined infrared and reflectron time-of-flight analysis. *Phys. Chem. Chem. Phys.* **2018**, *20*, 5435–5468.
- (59) Abplanalp, M. J.; Borsuk, A.; Jones, B. M.; Kaiser, R. I. On the formation and isomer specific detection of propenal (C₂H₃CHO) and cyclopropane (c-C₃H₄O) in interstellar model ices—a combined FTIR and reflectron time-of-flight mass spectroscopic study. *Astrophys. J.* **2015**, *814*, 45.
- (60) Szymańczyk, L. Analysis of common explosives in different solvents by nuclear magnetic resonance spectroscopy. *Cent. Eur. J. Energ. Mater.* **2014**, *11*, 129–142.
- (61) Infante-Castillo, R.; Pacheco-Londoño, L.; Hernández-Rivera, S. P. Vibrational spectra and structure of RDX and its ¹³C- and ¹⁵N-labeled derivatives: a theoretical and experimental study. *Spectrochim. Acta, Part A* **2010**, *76*, 137–141.
- (62) Iqbal, Z.; Suryanarayanan, K.; Bulusu, S.; Autera, J. R. *Infrared and Raman Spectra of 1,3,5-Trinitro-1,3,5-triazacyclohexane (RDX)*; National Technical Information Service, U.S. Department of Commerce: Springfield VA, 1972.
- (63) Alix, J.; Collins, S. The photochemistry of RDX in solid argon at 10 K. *Can. J. Chem.* **1991**, *69*, 1535–1538.

- (64) Kagann, R. H.; Maki, A. G. Infrared absorption intensities of nitrous acid (HONO) fundamental bands. *J. Quant. Spectrosc. Radiat. Transfer* **1983**, *30*, 37–44.
- (65) Kim, Y. S.; Kaiser, R. I. On the formation of amines (RNH₂) and the cyanide anion (CN[−]) in electron-irradiated ammonia-hydrocarbon interstellar model ices. *Astrophys. J.* **2011**, *729*, 68.
- (66) Kayi, H.; Kaiser, R. I.; Head, J. D. A computational study on the structures of methylamine–carbon dioxide–water clusters: evidence for the barrier free formation of the methylcarbamic acid zwitterion (CH₃NH₂+COO[−]) in interstellar water ices. *Phys. Chem. Chem. Phys.* **2011**, *13*, 11083–11098.
- (67) Socrates, G. *Infrared and Raman Characteristic Group Frequencies; Tables and Charts*, 3rd ed.; John Wiley and Sons: Chichester, U.K., 2001.
- (68) Mowrey, R. C.; Page, M.; Adams, G. F. Ab initio multireference configuration interaction study of CH₂NNO₂. HONO elimination vs NN bond fragmentation. *J. Chem. Phys.* **1990**, *93*, 1857–1864.
- (69) Zheng, W.; Jewitt, D.; Kaiser, R. I. Formation of hydrogen, oxygen, and hydrogen peroxide in electron-irradiated crystalline water ice. *Astrophys. J.* **2006**, *639*, 534–548.
- (70) Bennett, C. J.; Chen, S. H.; Sun, B. J.; Chang, A. H. H.; Kaiser, R. I. Mechanistical studies on the irradiation of methanol in extraterrestrial ices. *Astrophys. J.* **2007**, *660*, 1588–1608.
- (71) Fulvio, D.; Sivaraman, B.; Baratta, G. A.; Palumbo, M. E.; Mason, N. J. Novel measurements of refractive index, density and mid-infrared integrated band strengths for solid O₂, N₂O and NO₂:N₂O₄ mixtures. *Spectrochim. Acta, Part A* **2009**, *72*, 1007–1013.
- (72) Barney, W. S.; Wingen, L. M.; Lakin, M. J.; Brauers, T.; Stutz, J.; Finlayson-Pitts, B. J. Infrared absorption cross-section measurements for nitrous acid (HONO) at room temperature. *J. Phys. Chem. A* **2000**, *104*, 1692–1699.
- (73) Gerakines, P. A. S.; Greenberg, J. M.; van Dishoeck, E. F. The infrared band strengths of H₂O, CO and CO₂ in laboratory simulations of astrophysical ice mixtures. *Astron. Astrophys.* **1995**, *296*, 810–818.
- (74) Orloff, M. K.; Mullen, P. A.; Rauch, F. C. Molecular orbital study of the electronic structure and spectrum of hexahydro-1,3,5-trinitro-s-triazine. *J. Phys. Chem.* **1970**, *74*, 2189–2192.
- (75) Borges, I., Jr; Aquino, A. J. A.; Barbatti, M.; Lischka, H. The electronically excited states of RDX (hexahydro-1,3,5-trinitro-1,3,5-triazine): vertical excitations. *Int. J. Quantum Chem.* **2009**, *109*, 2348–2355.
- (76) Bergantini, A.; Góbi, S.; Abplanalp, M. J.; Kaiser, R. I. A mechanistical study on the formation of dimethyl ether (CH₃OCH₃) and ethanol (CH₃CH₂OH) in methanol-containing Ices and implications for the chemistry of star-forming regions. *Astrophys. J.* **2018**, *852*, 70.
- (77) Bergantini, A.; Maksyutenko, P.; Kaiser, R. I. On the formation of the C₂H₆O isomers ethanol (C₂H₅OH) and dimethyl ether (CH₃OCH₃) in star-forming regions. *Astrophys. J.* **2017**, *841*, 96.
- (78) Abplanalp, M. J.; Kaiser, R. I. Implications for extraterrestrial hydrocarbon chemistry: Analysis of ethylene (C₂H₄) and D4-ethylene (C₂D₄) ices exposed to ionizing radiation via combined infrared spectroscopy and reflectron time-of-flight mass spectrometry. *Astrophys. J.* **2017**, *836*, 195.
- (79) Turner, A. M.; Bergantini, A.; Abplanalp, M. J.; Zhu, C.; Góbi, S.; Sun, B.-J.; Chao, K.-H.; Chang, A. H. H.; Meinert, C.; Kaiser, R. I. An interstellar synthesis of phosphorus oxoacids. *Nat. Commun.* **2018**, *9*, 3851.
- (80) Frigge, R.; Zhu, C.; Turner, A. M.; Abplanalp, M. J.; Sun, B.-J.; Huang, Y.-S.; Chang, A. H. H.; Kaiser, R. I. Synthesis of the hitherto elusive formylphosphine (HCOPH₂) in the interstellar medium – a molecule with an exotic phosphorus peptide bond. *Chem. Commun.* **2018**, *54*, 10152–10155.
- (81) Abplanalp, M. J.; Gozem, S.; Krylov, A. I.; Shingledecker, C. N.; Herbst, E.; Kaiser, R. I. A study of interstellar aldehydes and enols as tracers of a cosmic ray-driven nonequilibrium synthesis of complex organic molecules. *Proc. Natl. Acad. Sci. U.S.A.* **2016**, *113*, 7727–7732.
- (82) Eckhardt, A. K.; Bergantini, A.; Singh, S. K.; Schreiner, P. R.; Kaiser, R. I. Formation of glyoxylic acid in interstellar ices: a key entry point for prebiotic chemistry. *Angew. Chem., Int. Ed.* **2019**, *58*, 5663–5667.
- (83) Abplanalp, M. J.; Góbi, S.; Bergantini, A.; Turner, A. M.; Kaiser, R. I. On the synthesis of chocolate flavonoids (propanols, butanals) in the interstellar medium. *ChemPhysChem* **2018**, *19*, 556–560.
- (84) Lossing, F. P.; Lam, Y.-T.; Maccoll, A. Gas phase heats of formation of alkyl immonium ions. *Can. J. Chem.* **1981**, *59*, 2228–2231.
- (85) Gallegos, E.; Kiser, R. W. Electron impact spectroscopy of ethylene sulfide and ethylenimine. *J. Phys. Chem.* **1961**, *65*, 1177–1182.
- (86) Arenas, J. F.; Otero, J. C.; Peláez, D.; Soto, J. CASPT2 Study of the decomposition of nitrosomethane and its tautomerization reactions in the ground and low-lying excited states. *J. Org. Chem.* **2006**, *71*, 983–991.
- (87) Dibeler, V. H.; Walker, J. A.; Liston, S. K. Mass spectrometric study of photoionization. VII. nitrogen dioxide and nitrous oxide. *J. Res. Natl. Bur. Stand., Sect. A* **1967**, *71*, 371–378.